Journal of Applied Physics

RESEARCH ARTICLE | MAY 15 2026

Frequency-sweep force volume AFM-IR: Decoupling infrared mapping from mechanical properties

J. Rojas ; C. Collange ; V. Phan ; P. Nickmilder ; Ph. Leclère ; P. De Wolf ; M. Wagner; A. Deniset-Besseau ; J. Mathurin ; A. Dazzi

J. Appl. Phys. 139, 194901 (2026)
https://doi.org/10.1063/5.0317307

Journal of Applied Physics ARTICLE pubs.aip.org/aip/jap

Frequency-sweep force volume AFM-IR: Decoupling infrared mapping from mechanical properties

Cite as: J. Appl. Phys. **139**, 194901 (2026); doi: 10.1063/5.0317307
Submitted: 17 December 2025 · Accepted: 25 April 2026 ·
Published Online: 15 May 2026

J. Rojas,[1,a)] C. Collange,[1] V. Phan,[2] P. Nickmilder,[3] Ph. Leclère,[3] P. De Wolf,[4] M. Wagner,[4] A. Deniset-Besseau,[1] J. Mathurin,[1] and A. Dazzi[1]

AFFILIATIONS

[1]Institut de Chimie Physique, Université Paris-Saclay—CNRS, 91400 Orsay, France
[2]Institut des Sciences Moléculaires d'Orsay, Université Paris-Saclay—CNRS, 91400 Orsay, France
[3]Laboratory for Physics of Nanomaterials and Energy (LPNE), Research Institute for Materials Science and Engineering, University of Mons, 7000 Mons, Belgium
[4]Bruker Nano Surfaces Division, Santa Barbara, California 93117, USA

[a)]**Author to whom correspondence should be addressed:** julien.rojas@universite-paris-saclay.fr

ABSTRACT

Infrared nano-spectroscopy by atomic force microscopy-infrared (AFM-IR) couples an atomic force microscope (AFM) to tunable infrared (IR) laser radiation to perform infrared signature mapping of complex samples at a nanometric spatial resolution. Recently, the new frequency-sweep force volume AFM-IR operating mode was introduced, offering a way to measure the full frequency response of the cantilever-sample system during IR mapping. Such operating mode enables to integrate the frequency-dependent IR signal over resonance modes, thus incorporating into the IR response the resonance line shape and hence the magnitude of the mechanical damping of the system. Unlike conventional resonance-tracking methods (as implemented in AFM-IR contact, tapping, and peak force tapping), the frequency-sweep force volume AFM-IR mode performs IR mapping without requiring active resonance adjustment. This makes it particularly suitable for mechanically heterogeneous samples with substantial frequency shifts and low signal-to-noise ratios. In this work, we present a systematic AFM-IR study on standard polymer samples to showcase the IR mapping capabilities of the frequency-sweep force volume mode compared to resonance-enhanced contact and resonance-enhanced force volume modes. This study highlights that frequency spectra are a crucial tool to evaluate the suitability of a specific resonance mode to perform IR mapping and thus to interpret AFM-IR data. Integrating the frequency response of the system furthermore allows to improve the IR contrast on heterogeneous regions.

I. INTRODUCTION

Infrared (IR) spectroscopy is a major tool for the molecular characterization of samples as it allows to access the molecular rotational and vibrational transitions at a spatial resolution down to about tens of micrometers. Samples exhibiting high chemical heterogeneity at small length scales have benefited from synchrotron-based IR techniques (e.g., Dartois *et al.*, 2018), which offer enhanced spatial resolution. However, conventional far-field spectroscopy techniques remain constrained by the diffraction limit, preventing the investigation of sub-micrometer scale heterogeneities. To overcome this limitation, the AFM-IR technique, which is an Atomic Force Microscopy (AFM) based technique, combines the high spatial resolution of the AFM and the chemical identification capability of the infrared (IR) spectroscopy. For 20 years, this technique has continuously evolved and pushed the boundaries of detection sensitivity and spatial resolution (Dazzi *et al.*, 2005 and Mathurin *et al.*, 2022). The main advantage of the AFM-IR technique is its robust, reliable, model-free and hence user-friendly operation, which has led

to its widespread adoption as the prevalent technique for nanoscale infrared imaging and spectroscopy.

The original AFM-IR technique was implemented in AFM contact mode where the infrared light source (a free electron laser) was pulsed at a repetition rate off-resonant with the AFM cantilever (Dazzi *et al.*, 2005). While this setup allowed to improve the lateral resolution down to tens of nanometers, the sensitivity was relatively low. To address this limitation associated with low signal-to-noise ratios, contemporary AFM-IR methods boost the sensitivity by employing resonance enhancement. The laser repetition rate is now matched with one of the cantilever resonance frequencies for homodyne detection [such as in contact mode (Lu *et al.*, 2014) or peak-force tapping mode (Wang *et al.*, 2020)], or a fixed frequency mixing relationship is maintained for heterodyne detection [such as in tapping mode (Dazzi *et al.*, 2025) or surface sensitive mode (Mathurin *et al.*, 2022)]. Under these conditions, the capabilities of the technique are greatly improved, reaching monolayer films sensitivity [Lu *et al.*, 2014 (contact), Dazzi *et al.*, 2025 (tapping)]. Tapping mode and peak-force IR implementations are preferred on fragile or soft samples, as they suppress the shear force present during contact mode operation and allow us to preserve the sample integrity (Dazzi *et al.*, 2025; Mathurin *et al.*, 2018; Tuteja *et al.*, 2018; and Wang *et al.*, 2022). To compensate for resonance shifts induced by variations in the sample's mechanical properties, resonance tracking mechanisms are commonly applied. Recently, the frequency-sweep force volume operating mode, based on force volume measurements, was introduced (Wagner *et al.*, 2025). It performs IR imaging without applying shear forces during the tip scan and does not require the use of a resonance tracking mechanism inherent to classic resonance-enhanced and tapping operating modes. This is achieved by not measuring at a single laser repetition rate but rather sweeping over (at least) one cantilever resonance while the tip is held stationary on the sample area of interest. Inquiring into the IR response over the resonance line shape incorporates damping of the resonance mode into the IR absorption, which has not yet been studied in much detail. Such an approach should allow to decouple the IR absorption and the mechanical properties impacting the signal and render this relatively recent frequency-sweep force volume AFM-IR modality an interesting subject for investigation.

In this paper, we propose to compare the IR mapping performances of three different contact AFM-IR operating modes, the contact resonance-enhanced mode (RE), resonance-enhanced force volume mode (REFV), and the frequency-sweep force volume mode (FSFV). We performed AFM-IR mapping with those three modes on two different polymer blend samples to underline their advantages and limitations with the exact same cantilever. We aim at establishing the best suited operating mode depending on the user's needs and the sample's properties. The current study is focused on IR imaging, not spectroscopy, since frequency sweeps at each wavenumber of a spectrum have not yet been technically implemented in FSFV. Tapping AFM-IR was not included in this study as it is a surface-sensitive technique, with a probing depth significantly lower than contact methods, relying on a non-linear frequency mixing (heterodyne) that does not allow a direct comparison with the homodyne detection scheme of contact operating modes. Furthermore, any methods relying on resonance tracking are likely to be impacted by mechanical variations within samples. Tapping AFM-IR, which requires to track the resonance of two eigenmodes of the cantilever (Dazzi *et al.*, 2025), can thus be affected by frequency tracking artifacts and cannot decouple IR and mechanical contributions to the AFM-IR signal.

II. MATERIAL AND METHODS

A. Principle and experimental setup

1. Principle

Contact-based AFM-IR techniques rely on the coupling of an AFM tip with light from a tunable infrared pulsed laser illuminating the sample below the tip. When the laser wavelength matches an absorption band of the sample, the sample locally expands and relaxes, at the repetition rate of the laser. This mechanical constraint is probed by the AFM tip. The efficient detection of the IR signal relies on the appropriate tuning of the repetition rate of the laser to a resonance mode of the cantilever, thus ensuring resonance enhancement of the IR signal. The behavior of the resonance is determined by the complex tip–sample interactions. In a simplified model, the amplitude of the resonant mode n can be described by the characteristic function of a damped simple harmonic oscillator (hereafter DSHO),

$$A(f) = \frac{B_n(v)}{\sqrt{\left(\omega_n^2 - (2\pi f)^2\right)^2 + (2\pi f \Gamma)^2}}, \tag{1}$$

with $\omega_n = 2\pi f_n$ being the natural angular frequency of the mode, Γ being the damping coefficient, and B_n being an amplitude factor depending on the response of the cantilever and the absorption of the sample at the wavenumber v. The damping Γ reflects both the dissipative nature of the medium probed and of the resonant mode of the cantilever (Rabe, 2006). It is proportional to the full width at half maximum (FWHM) of the resonance mode. Within the limit $\frac{\Gamma}{\omega_n} \ll 1$, one has FWHM $\approx \sqrt{3}\Gamma/2\pi$. The integral of the amplitude signal centered around ω_n is a measure of the energy of the mode. Given a cantilever of mass density ρ, section A, and length L, the natural frequency f_n depends on the stiffness of the cantilever k_c and the normalized eigenvalue of the cantilever X_n (Dazzi *et al.*, 2010),

$$f_n = \frac{1}{2\pi} X_n^2 \sqrt{\frac{k_c}{3\rho A L}}. \tag{2}$$

The value of X_n depends on the contact interaction and can be expressed as a function of the eigenvalues of the cantilever in the clamped and free configurations, X_n^c and X_n^f respectively,

$$X_n = \frac{\left(X_n^c - X_n^f\right)}{1 + \frac{k_c L^2}{3 k_x H^2}\left(a_n X_n^c - X_n^f\right)} + X_n^f, \tag{3}$$

with k_x being the lateral stiffness of the probe–sample interaction and H being the tip height. The value of f_n is, thus, driven by the local mechanical properties of the sample through k_x, as a soft material ($k_c \gg k_x$) is expected to induce a lower natural angular frequency than a stiffer one ($k_c \ll k_x$). The value of f_n is bounded between the natural frequencies of the clamped and free beams through X_n. Since $\Delta X_{n,c-f} = (X_n^c - X_n^f)$ decrease with increasing n (Dazzi *et al.*, 2010), the frequency shift for materials of different stiffness decreases for higher modes. Given the dependence of the resonance frequency on the mechanical properties of a sample, contact-based AFM-IR techniques require a protocol to accurately tune the laser repetition rate to the resonant mode of the AFM cantilever during data acquisition.

Additionally, forces deriving from the nature of the tip–sample contact can affect the eigenmodes of the cantilever. For instance, the shear force applied to the surface while scanning the tip on the sample's surface can enhance the intensity of specific eigenmodes of the cantilever. Such shear force can also damage soft samples (as shown in Sec. III B). Until the development of force volume modes, classical contact resonance-enhanced AFM-IR (RE) was the principal contact AFM-IR mode. As developed below, RE relies on the measurement of the maximum amplitude of the light induced oscillations of the cantilever and is not sensitive to their damping. Resonance-enhanced force volume (REFV) and frequency-sweep force volume (FSFV) AFM-IR operate without laterally scanning the tip during the AFM-IR data acquisition, suppressing the effect of shear forces. While REFV also relies on the measurement of the maximum amplitude of the oscillations of the cantilever, FSFV records a frequency spectrum that gives access to the complete set of parameters of the eigenmodes of the cantilever (including damping effects).

In order to evidence the capabilities of force volume AFM-IR, we performed a series of experiments on standard samples using the classical RE AFM-IR in comparison to REFV and FSFV AFM-IR.

2. Resonance-enhanced AFM-IR (contact)

In the contact resonance-enhanced AFM-IR operating configuration, an AFM tip is scanned over the sample surface in constant contact allowing to derive simultaneously topographic and infrared absorption maps at a given wavenumber and repetition rate. Absorption is measured as the amplitude output of a Lock-In amplifier locked to the laser repetition rate. Cantilever frequency shifts induced by variations of the local mechanical properties of the sample are tracked with a phase-locked loop (PLL). The principle of the PLL is to change the laser repetition frequency to continuously match the local contact resonance while scanning, thanks to the tracking of the resonance phase by a feedback loop (Dazzi *et al.*, 2025). Scanning the tip over the surface creates shear forces that can damage soft samples and that can impact the intensity of specific eigenmodes of the cantilever.

3. Resonance-enhanced and frequency-sweep force volume (REFV and FSFV) AFM-IR

Force volume AFM-IR modes [Wagner *et al.* (2025)] (FSFV and REFV) use an intermittent contact where, at each sampled point, the AFM tip follows the sequence visualized in Fig. 1(a): approach, hold contact and retract, while movement to the next position on the sample occurs when not in contact with the surface. Mechanical properties of the sample such as stiffness, elastic modulus, and adhesion can be retrieved from the approach and retract curves while the hold time is used to probe the IR response of the sample. This method allows to image the sample's surface without applying shear forces, which significantly enhances the preservation of the sample. As with all pixel-based imaging modes, the accurate mapping of a surface strongly depends on spatial sampling, i.e., the number of measured points per line. Under-sampling might result in unrealistic topographic and IR contrasts and might also affect the accuracy of phase tracking in REFV.

In REFV, during the hold time, the laser illuminates the sample at a given wavelength and at a pulse rate matching a resonance frequency of the cantilever. If the sample is absorbing at the chosen wavelength, IR absorption during hold contact is measured in the same way as in the classical resonance-enhanced AFM-IR technique [Fig. 1(d)]. A PLL is used to track the shift of the resonance frequency of the cantilever, resulting in a constant phase in Fig. 1(e).

In FSFV, during the hold time, the laser illuminates the sample at a given wavenumber and its repetition rate is scanned over a user-defined frequency range. This allows one to record a frequency spectrum of the cantilever [see Fig. 1(h)] at each sample position, directly reflecting the behavior of the tip–sample interaction. Output data for FSFV are data cubes with X and Y representing the plane coordinates and Z the frequency axis. The hold time can be increased as required to cover a large frequency range and simultaneously record signals arising from multiple resonant modes. No PLL is used in FSFV as the resonant frequencies can be extracted from the frequency spectra during data processing. Acquiring the frequency spectra of the cantilever also allows one to quantify the quality factor of each mode and thus to provide an extensive description of the thermo-mechanical response of the system given a set of contact conditions. Therefore, FSFV is the more suitable mode to derive IR chemical mapping decoupled from mechanical influence. In this study, we consider IR maps obtained with FSFV as reference data. Still, it is important to note that FSFV acquisitions on large frequency ranges are significantly more time-consuming than REFV and RE modes, as apparent from the example in Fig. 1.

B. AFM-IR experiments

AFM-IR experiments were performed with a Dimension IconIR instrument from Bruker, equipped with an IR tunable QCL laser (Daylight Solutions) of spectral range 1900–900 cm^{-1}. We used a NanoSensors cantilever PPP-CONTAu with a spring constant of 0.2 N/m and a deflection sensitivity of 160 nm/V. All the AFM-IR acquisitions were performed with a 32 nm indentation setpoint, resulting in an applied force of about 6.4 nN. The laser pulse width was set to 100 ns, and the laser repetition rate varied from 20 to 2000 kHz, corresponding to duty cycles ranging from 0.002 to 0.2. The laser power was set to a fixed value for a given sample, either 2.3% or 4.9%. All acquisitions were performed

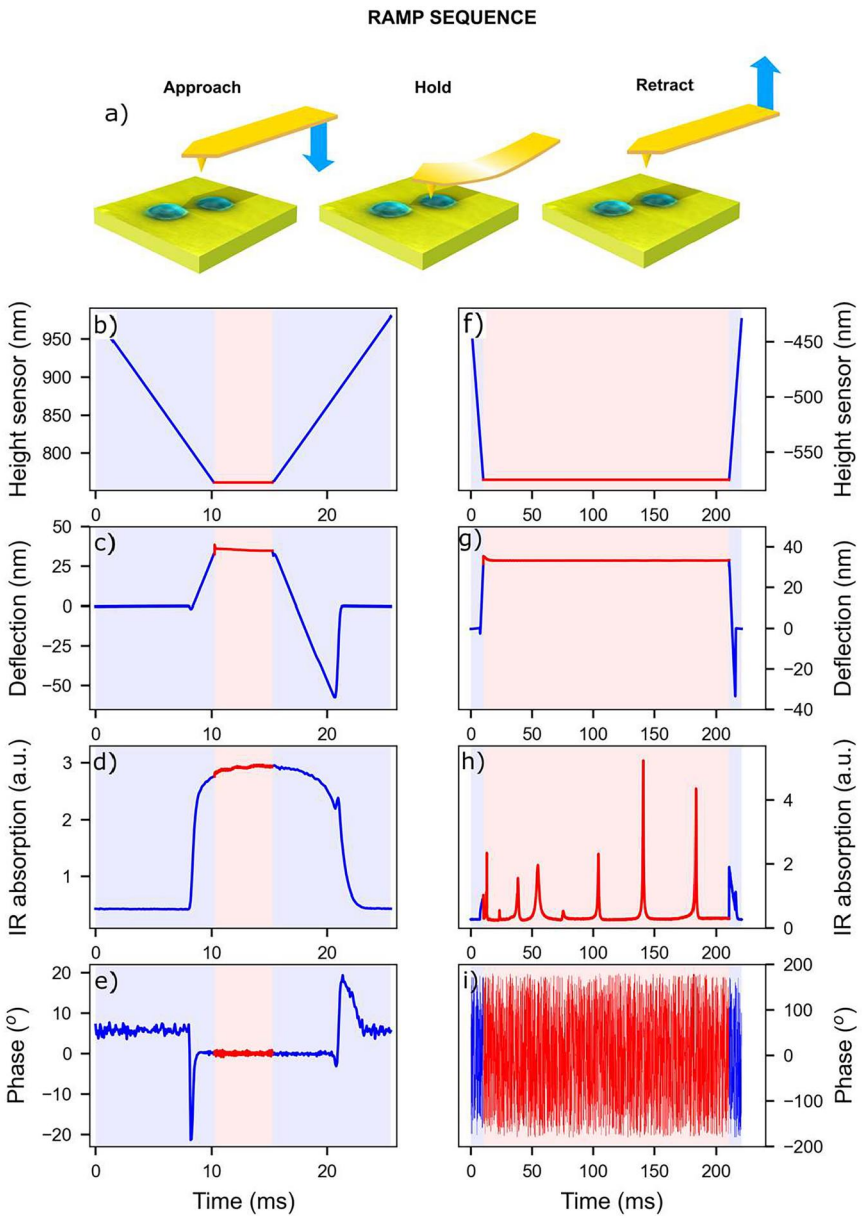

FIG. 1. Operating sequence of the force volume AFM-IR modes, REFV (left) and FSFV (right), representing a single FV cycle of approach, hold and retract as visualized in panel (a). (b) and (f) The cantilever is approached to the sample's surface as shown by the decrease in height of the cantilever. (c) and (g) The deflection of the cantilever increases until reaching the user-defined deflection setpoint of 32 nm. The setpoint is then held, using regular contact-mode type deflection feedback, during a user-defined hold time (5 ms in REFV and 200 ms in FSFV here). (d) In REFV, the laser is emitting at a repetition rate tuned to a cantilever resonance and causing a constant IR absorption signal during the hold segment. (e) Resonance frequency shifts are compensated with a PLL that maintains a zero-phase. (h) In FSFV, the repetition rate of the laser is swept over a user-defined frequency range providing a frequency spectrum at the held position and covering multiple resonant modes of the tip–sample system. (i) The PLL tracking is not active in FSFV. Finally, after the hold segment the cantilever is retracted before moving to the next sample position.

on $10 \times 10\ \mu m^2$ regions with 256×256 pixels. RE acquisitions were performed with a scan rate (number of lines per second) of 0.3 Hz, corresponding to a scan speed of 3 μm/s. For REFV and FSFV acquisitions, the ramp rate, which provides the time to perform the complete ramp sequence without taking into account the hold time sequence, was set to 48.8 Hz (10.2 ms for each approach and retract ramp), and each ramp was sampled over 128 points. Ramp sizes were set to 200 and 150 nm for REFV and FSFV, respectively, leading to approach/retract speeds of 20 and 15 μm/s. The hold time of REFV acquisitions was 5 ms. For FSFV acquisitions, the hold time lasted 200 ms, during which the repetition rate of the laser was swept from 20 to 2000 kHz with 2500 sampling points. For each frequency increment of 0.792 kHz, the IR signal was integrated N times over 0.08 ms periods (12.5 kHz bandwidth). The number of integration N is given by the ratio of the repetition rate over the bandwidth and increases with the repetition rate. Given the ramp rate and the hold time of REFV and FSFV acquisitions, the cycle durations per pixel are 25 and 220 ms corresponding to about 6 and 56 s per line. For both RE and REFV acquisitions, the frequency shifts were bounded to ±10 kHz around the resonance frequency. The typical time for the PLL to lock to zero phase is 0.5 ms, as shown

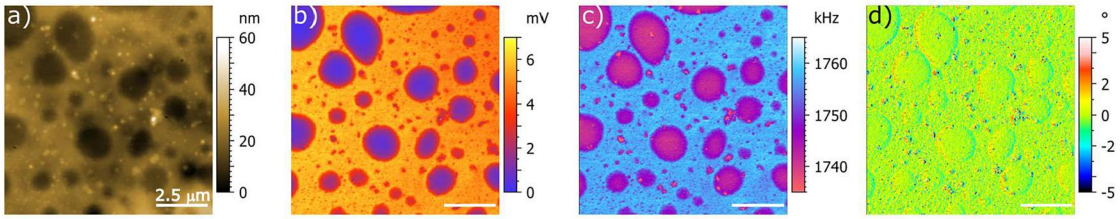

FIG. 2. Two-dimensional output of RE imaging for the PS-PMMA sample at 1730 cm^{-1} using the 1750 kHz cantilever mode. The sample is made of polystyrene beads embedded in a poly(methyl methacrylate) matrix (see Sec. II). (a) Topographic map, (b) IR amplitude map at 1730 cm^{-1}, (c) resonant frequency map, (d) phase map. The phase is kept near zero by the PLL.

in Fig. 1 and by Wagner *et al.*, (2025). In the following, we restrict ourselves to AFM-IR imaging to evaluate the impact of frequency sweeps in FSFV on image contrast at single wavelengths, expecting the results to hold true in spectroscopy covering multiple wavelengths.

C. Data format and data processing

Data derived from RE imaging at 1730 cm^{-1} on a PS-PMMA sample are shown in Fig. 2. Figure 3 is an illustration of the dataset obtained from the FSFV acquisition on the same sample and at the same wavelength. It displays the different quantities related to the AFM-IR signal. Thanks to its comprehensiveness, the FSFV dataset can be used to describe data obtained in the RE and REFV modes.

1. Classical resonance-enhanced AFM-IR

In RE, the output data are two-dimensional maps of the topography [Fig. 2(a)], the deflection, the IR-induced signal's amplitude [Fig. 2(b)], the detection frequency [Fig. 2(c)], and the phase of the signal from the PLL tracking [Fig. 2(d)]. The sample consists of polystyrene (PS) beads embedded in a poly(methyl methacrylate) (PMMA) matrix. At the chosen wavelength of 1730 cm^{-1}, only the PMMA matrix absorbs as shown in Fig. 2(b). The accuracy of the phase tracking by the PLL can be monitored by looking at the frequency and phase maps [Figs. 2(c) and 2(d)]. A flat phase map is expected for accurate tracking. The 1750 kHz resonant mode of the cantilever selected for the RE measurement is presented in Fig. 3(g) (as part of the FSFV dataset) and is characterized by a central frequency, an amplitude, an FWHM (see Sec. II A 1), and a small amplitude offset due to the instrumental

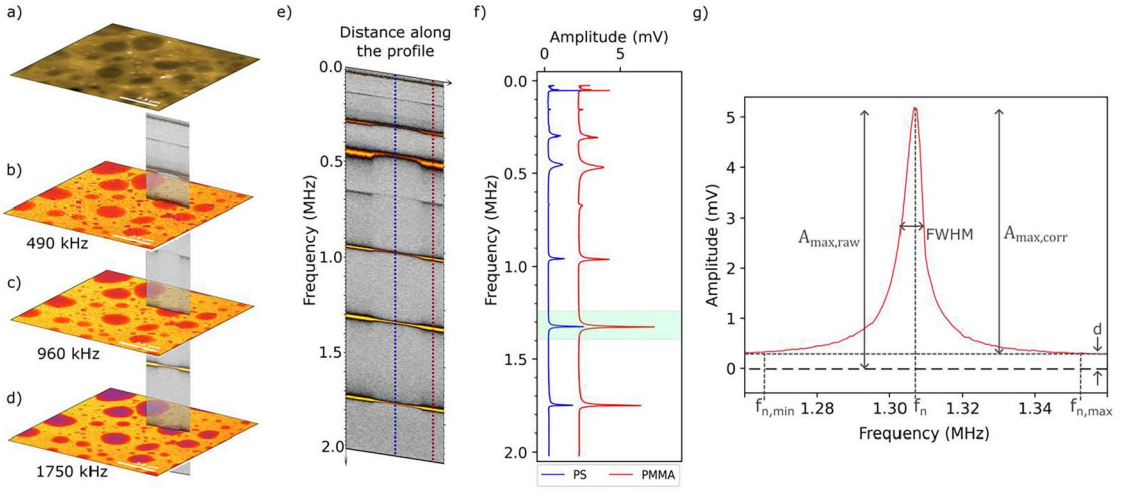

FIG. 3. FSFV data cube of a PS-PMMA sample acquired at 1730 cm^{-1}. Each pixel of the sample contains a broad laser repetition frequency sweep over many cantilever resonances. (a) Topographic image of the sample derived from the force-curves. (b), (c) and (d) absorption maps extracted as IR peak amplitudes at the cantilever resonance frequencies 490, 960, and 1750 kHz. (e) Frequency slice along a linear profile going through a PS bead in the PMMA matrix. (f) Frequency profiles along the blue (PS bead) and red doted lines (PMMA matrix) in (e). (g) Zoom in on the red frequency spectrum around 1320 kHz. The peak is characterized by the curve offset d, its position f_n, its FWHM and its maximum amplitude $A_{max,raw}$ (raw amplitude) and $A_{max,corr}$ (offset-corrected). The lower and upper integration limits for FSFV data are $f_{n,min}$ and $f_{n,max}$.

noise of the detection system. Importantly, RE measures the maximum amplitude of the cantilever mode [$A_{1730,PMMA}$ in Fig. 3(g)] and is not capable to detect its damping or the instrumental offset.

2. Resonance-enhanced force volume AFM-IR

For REFV, the output data for the topography and the deflection are 2D maps similar to the ones obtained in RE. The IR amplitude and phase are averaged over the hold time during which the phase tracking is active, resulting in 2D maps. No further advanced data treatment is required to extract the IR signal. The phase map can be used to check the quality of the PLL correction. As for RE, REFV provides a measure of the maximum IR induced amplitude of a mode, $A_{max,raw}$ in Fig. 3(g), but does not separate from the IR response the effect of damping and the instrumental (noise) offset. In addition, maps of mechanical properties, such as adhesion and modulus, are also acquired (Wagner *et al.*, 2025). REFV AFM-IR maps are displayed in Fig. 4 and Appendix B.

3. Frequency-sweep force volume AFM-IR

Frequency-sweep force volume data cubes display the frequency spectra associated with each pixel of the sample surface. We visualize the variation in the frequency spectra by drawing a 3 μm-long profile across a region with heterogeneous chemical and mechanical properties, as shown in Fig. 3. We obtain a color map representing the 2D position-frequency slice displaying the IR amplitude as a function of the repetition rate of the laser along the selected section profile [Fig. 3(e)]. In contrast to the IR amplitude data output provided by other acquisition modes, FSFV data cubes provide raw data on which different advanced data treatments can be performed to extract a comprehensive set of parameters of the tip–sample interaction. We processed the data presented in this article with an in-house processing software dedicated to the in-depth analysis of FSFV data cubes (Collange *et al.*, 2025 and Appendix E). First, we applied a smoothing kernel to the frequency spectra and we subtract an offset d at each pixel. The offset was constant over individual data cubes and is likely an instrumental baseline. We subsequently defined a frequency range $\Delta f_n = f_{n,max} - f_{n,min}$ covering the resonance frequencies of interest (e.g., f_n = 490, 960, 1750 kHz for PS-PMMA), ensuring that the user-defined frequency range was wide enough to cover the frequency shift induced by the heterogeneous stiffness of the sample and did not include modes other than the one of interest. The peak value of the mode, $A_{max,corr}$ in Fig. 3(g), is then determined either by a direct measurement or by a fitting routine with the DSHO model [Eq. (1)] and is displayed in the IR amplitude map. Conversely to REFV, in FSFV, the peak value of the mode is offset-corrected: $A_{max,corr} = A_{max,raw} - d$. Examples of these amplitude maps are shown in Figs. 3(b)–3(d) for the three selected resonances of 490, 960, and 1750 kHz, respectively. The parameter f_n can be visualized as well in a two-dimensional map equivalent to the resonance frequency map in RE of Fig. 2(c). However, access to the full line shape of (at least one) resonance provides rich additional information beyond the peak amplitude and center frequency that RE or REFV also deliver. The processing software also extracts Γ (damping, proportional to the FWHM), a unique feature resulting from the frequency sweep. Furthermore, this damping can be incorporated in an IR absorption response when integrating the amplitude signal over the frequency range Δf for an integrated IR amplitude map. In the case of a DSHO profile and with $\frac{\omega_n}{\Gamma} \gg 1$, the integrated amplitude is given by (Appendix E)

$$\tilde{A} = \int_{f_n-\Delta f}^{f_n+\Delta f} A_{corr}(f)df = \int_{f_n-\Delta f}^{f_n+\Delta f} (A_{raw}(f) - d)df = A_{max,corr}(\Gamma) \cdot \Gamma \cdot \alpha\left(\frac{\Delta f}{\Gamma}\right), \quad (4)$$

where $\alpha(\Delta f/\Gamma)$ is a positive increasing function of $\Delta f/\Gamma$. Noticeably, the integrated amplitude is proportional to the product of the maximum amplitude and the damping.

III. CASE-STUDY: CONTRAST AND FREQUENCY TRACKING

Through two case-studies, we aimed at assessing the capabilities of REFV and FSFV to (i) evidence IR contrast in chemically heterogeneous samples and (ii) operate on fragile, mechanically heterogeneous samples. We tested the first point by analyzing the previously mentioned sample consisting of polystyrene (PS) droplets of varying sizes embedded in a 1.9 μm thick poly(methyl methacrylate) (PMMA) matrix of respective Young's moduli 2.7 and 3.1 GPa [the same sample as investigated in Dazzi *et al.*, (2024)]. This sample was made of two materials with similar mechanical properties but distinct IR signatures, deposited on a silicon substrate. We tested the second point using a sample made of 70 nm-thick low-density polyethylene (LDPE) droplets with a Young's modulus roughly one order below the modulus of the surrounding 35 nm-thick PS matrix. This sample is from Bruker (P/N: PS-LDPE-12M) and was prepared by spin-casting on silicon (Wagner *et al.*, 2025). We confirmed in Fig. 14 in Appendix D that REFV spectra of LDPE droplets do not contain contributions from PS, i.e., the LDPE droplets are embedded and do not sit on top of PS which would have contributed otherwise given our extended probing depth. Contrary to the PS-PMMA sample, the PS-LDPE sample is characterized by the heterogeneous mechanical properties of its two constituents.

A. PS-PMMA

We performed AFM-IR mapping at 1730 cm^{-1}, which corresponds to the carbonyl absorption band of PMMA, using the three acquisition methods, on the same area of the PS-PMMA sample. To study the responses of the AFM-IR techniques at different cantilever modes, we reproduced the RE and REFV imaging at eight different repetition rates, corresponding to the eigenmodes of the cantilever used: 50, 160, 310, 490, 675, 960, 1320, and 1750 kHz. For a direct comparison, we carried out a single FSFV scan with a 20–2000 kHz frequency sweep. The resulting 2D maps are displayed in Fig. 4 for the 1320 kHz mode. Topographic images are shown in (a)–(c), evidencing the flat nature of the sample with a typical height variation of 10–15 nm between PS

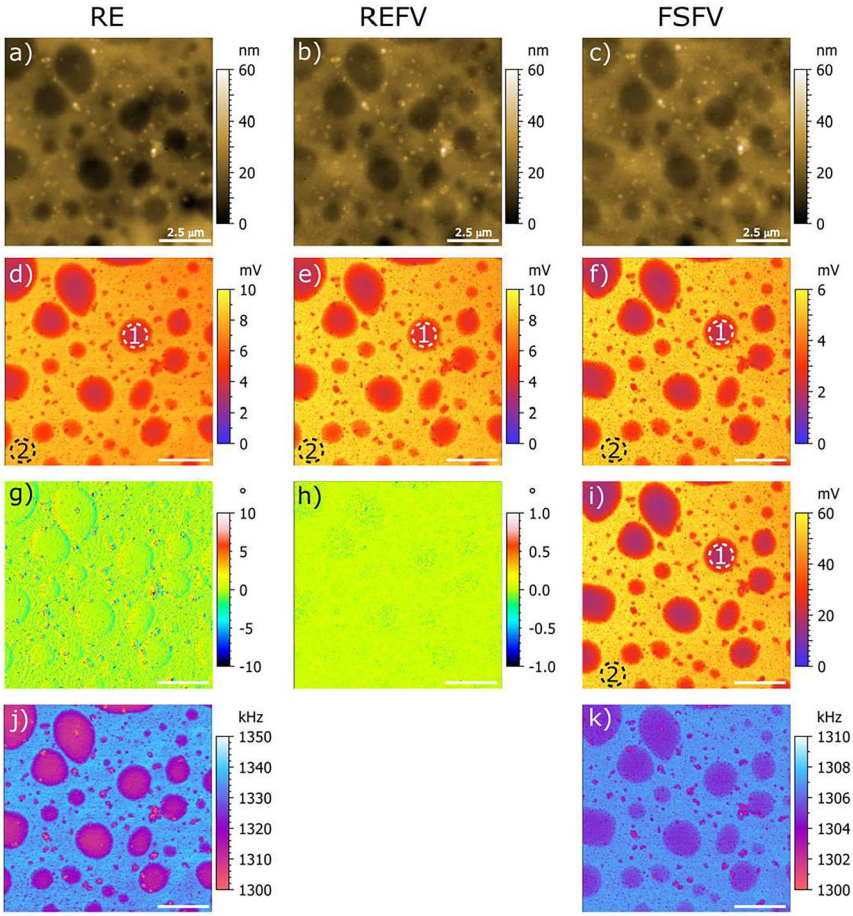

FIG. 4. Maps of the same area derived from RE, REFV, and FSFV modes on the PS-PMMA sample at the ∼1320 kHz mode. First column (RE): (a) topography, (d) maximum IR amplitude at 1730 cm^{-1}, (g) phase and (j) frequency for RE-contact. Second column (REFV): (b) topography, (e) maximum IR amplitude at 1730 cm^{-1} and (h) phase for REFV. Third column (FSFV): (c) topography, (f) maximum IR amplitude, (i) integrated IR amplitude at 1730 cm^{-1}, and (k) frequency for FSFV. Dotted circles indicate the two regions of interest, which were used to compute the chemical contrasts.

and PMMA. Images (d)–(f) display the maps of the maximum or peak amplitudes of the 1320 kHz mode, respectively, derived from the RE, REFV, and FSFV data (note that FSFV peak amplitudes are offset-corrected). Image (i) is the integrated amplitude signal between 1300 and 1340 kHz from FSFV. Images (j) and (k) are the maps of the resonant frequency derived from RE and FSFV. As FSFV and REFV have an identical mechanical interaction, the frequency map derived from FSFV is expected to be representative of the one for REFV. Unfortunately, a direct acquisition of the REFV frequency map was not supported by the software, and this information could not be retrieved in post-processing. Phase maps derived from the PLL tracking are shown in (g) and (h) for RE and REFV.

Figures 4(j) and 4(k) show that shifts of the resonance frequency of the cantilever over PS and PMMA are of about 20 kHz in RE and of about 2 kHz in FSFV. The larger shift observed in the RE map results from the shear force applied to the tip while scanning which modifies the expression of the resonance frequency. In REFV and FSFV, the absence of shear forces on the tip implies reduced frequency shifts when transitioning from PS to PMMA. Such a limited shift allows a better tracking of the resonance in REFV, as illustrated by the phase maps. While the phase variations in RE range from −5° to +5° [Fig. 4(g)], they are limited to −0.8° to +0.8° for REFV [Fig. 4(h)].

We aim at quantifying the IR contrast between a PS bead and the PMMA matrix given by RE, REFV, and FSFV to assess the sensitivity of the different acquisition modes since the ability to appropriately measure IR contrasts is one of the major criteria to evaluate AFM-IR mapping abilities. We thus defined two regions of interest (ROIs) drawn with dashed circles on the amplitude maps of Fig. 4. Those regions, labeled 1 and 2, are located on a PS bead and the PMMA matrix, respectively, and do not include the bead/matrix boundary as the behavior of AFM-IR signal at the bead/matrix boundary appears to be complex and is not addressed here. Although maximum amplitude maps are displayed with the same color scale, they shall not be compared directly as the FSFV map is offset-corrected. To further compare the ability of AFM-IR techniques to evidence the chemical contrast of the two ROIs, we introduce the average amplitude of a ROI containing N pixels at a wavenumber ν,

$$a_\nu(\mathrm{ROI}) = \frac{1}{N}\sum_{i=1}^{N} A_{\max,i}\left(\frac{\mathrm{mV}}{\mathrm{pixel}}\right). \quad (5)$$

The amplitude ratio $R_{v,\,1-2}$ is then defined as the ratio of the average amplitude of ROIs 1 and 2,

$$R_{v,\,1-2} = \frac{a_v(\mathrm{ROI1})}{a_v(\mathrm{ROI2})}. \tag{6}$$

Subsequently, we define the IR contrast C of the 2D maximum amplitude map, at 1730 cm^{-1}, as

$$C = (1 - R_{1730,\,1-2}) \times 100\%\,. \tag{7}$$

For RE and REFV, the peak IR amplitude and, thus, the contrast are not offset-corrected ($A_{max} = A_{max,raw}$). For FSFV, the peak IR amplitude and the contrast are offset-corrected ($A_{max} = A_{max,corr}$).

Similarly, for integrated amplitude maps, we define the average integrated amplitude of a ROI containing N pixels as

$$\tilde{a}_v(\mathrm{ROI}) = \frac{1}{N}\sum_{i=1}^{N}\tilde{A}_i \left(\mathrm{mV}\cdot\frac{\mathrm{Hz}}{\mathrm{pixel}}\right), \tag{8}$$

which can be expressed as a function of the maximum amplitude $A_{max,corr,i}$ and the damping coefficients Γ_i of pixel i,

$$\tilde{a}_v(\mathrm{ROI}) = \frac{1}{N}\sum_{i=1}^{N}\alpha\left(\frac{\Delta f}{\Gamma_i}\right)\cdot A_{\mathrm{max,corr},i}\cdot\Gamma_i\,. \tag{9}$$

The positive increasing function $\alpha(\Delta f/\Gamma)$ is discussed and computed in Appendix E. The integrated amplitude ratio and contrast between two amplitude ratios 1 and 2 are, thus, defined as

$$\tilde{R}_{v,1-2} = \frac{\tilde{a}_v(\mathrm{ROI1})}{\tilde{a}_v(\mathrm{ROI2})}, \tag{10}$$

$$\tilde{C} = (1 - \tilde{R}_{1730,1-2}) \times 100\%\,. \tag{11}$$

Noticeably, the integrated amplitude ratio $\tilde{R}_{v,1-2}$ differs from the amplitude ratio $R_{v,1-2}$ depending on the magnitude of the damping Γ. Using these definitions, we can assess the chemical contrast between a PS bead and the PMMA matrix, on the amplitude maps at different repetition rates of the IR laser. Within this approach, we consider that FSFV integrated amplitude maps provide the most accurate IR contrasts, decoupled from mechanical damping, not affected by shear forces, and offset-corrected. Although the contrast can be calculated for all the resonance modes, the shape of a resonance mode has to be assessed on the frequency sweep data to ensure its accuracy/validity.

Figure 5 displays the different contrasts derived from the two ROIs shown in Fig. 4 at the different repetition rates for all three AFM-IR acquisition methods. Amplitude contrasts derived from RE (hereafter C_{RE}), REFV (hereafter C_{REFV}), and FSFV (hereafter C_{FSFV}) are shown with black circles, green squares, and red squares, respectively. Integrated amplitude contrasts derived from FSFV (hereafter $\tilde{C}_{FSFV}$) are shown with blue diamonds. Figure 5 shows that $\tilde{C}_{FSFV}$ tends to be higher than C_{FSFV} and C_{REFV}. Differences between $\tilde{C}_{FSFV}$ and C_{FSFV} arise from the behavior of

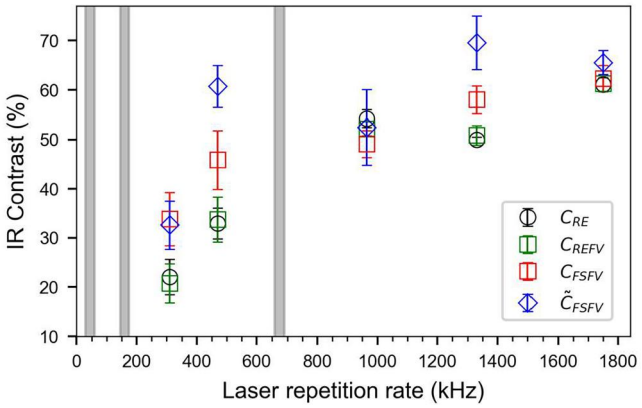

FIG. 5. PS-PMMA contrast at 1730 cm^{-1} measured for different laser repetition rates. Black circles, green squares, and red squares are derived from the maximum amplitude maps of RE, REFV, and FSFV. Blue diamonds are derived from the integrated amplitude maps of FSFV. Data points at 50, 160, and 675 kHz are not displayed (but substituted with gray vertical lines) as the low signal to noise ratio at those frequencies prevented data processing.

the damping coefficient ratio Γ_1/Γ_2 of the resonant modes, while offset subtraction was applied in both cases and hence cannot be responsible for the dissimilarity. For the three highest modes at 960, 1320, and 1750 kHz, $\tilde{C}_{FSFV}$ is higher than C_{FSFV} or equal within error, indicating that $\Gamma_1/\Gamma_2 \leq 1$, i.e., the damping coefficient of PMMA is higher than or equal to the damping coefficient on PS. The three modes can be accurately modeled by a DSHO profile verifying the condition $\Gamma/\omega_n \ll 1$, with damping coefficients ranging from 26 to 32 kHz on PMMA and 24 to 27 kHz on PS. The mode at 490 kHz can also be modeled with a DSHO and verifies $\tilde{C}_{FSFV} > C_{FSFV}$ indicating that $\Gamma_1/\Gamma_2 \leq 1$. However, the average damping coefficients derived from this mode are 84 and 68 kHz for PMMA and PS, 2.5–3.2 times higher than the ones derived from the modes at 960, 1320, and 1750 kHz. We attribute such a difference to the larger probing depth of 200–400 nm at 490 kHz (Dazzi *et al.*, 2024) that makes the measurement sensitive to the substrate nature. The presence of the silicon substrate influenced our AFM-IR tomography experiments before (Dazzi *et al.* 2024) on the same sample of a 1.9 μm thick PMMA layer with embedded ~100 nm thick PS islands at the surface. Damping coefficients measured by AFM-IR at 490 kHz might, thus, convolute damping coefficients of the polymer sample and the silicon substrate. Therefore, contrasts at this resonant mode might not be representative of the PS-PMMA properties. The resonant mode at 310 kHz cannot be modeled by a single DSHO profile as it results from the combination of two distinct resonant modes (Fig. 7 in Appendix A). Thus, although IR contrast values can be derived from the integration of the FSFV data at 310 kHz, disentangling the contributions of the different modes is challenging, preventing an accurate interpretation of the IR contrasts at 310 kHz. Finally, the modes at 50, 160, and 675 kHz (represented by gray vertical lines in Fig. 5) are characterized by a low signal-to-noise ratio that prevents advanced data processing (Fig. 7 in Appendix A).

Noticeably, C_{FSFV} is higher than C_{REFV} for the modes at 310, 490, and 1320 kHz. This quasi-systematic trend may be attributed to uncertainties in the resonance tracking by the PLL. Although the offset subtraction on the FSFV data leads to a slight increase of C_{FSFV} compared to C_{REFV}, it is not large enough to explain the observed difference.

Values of C_{RE} are in good agreement with values of C_{REFV}, indicating that the phase-tracking was efficient despite the higher frequency shifts induced by the shear forces (Fig. 4).

In summary, on the PS-PMMA sample, FSFV allowed to visualize the resonant modes of the tip–surface interaction that are best suited for achieving IR mapping corrected from damping influence and amplitude offsets, which led to, on average, an enhancement of the IR contrast compared to REFV and RE. The suppression of shear forces in FSFV and REFV simplified the nature of the interaction and limited the mechanical constraints on the sample even though the sample was not visibly damaged during the RE acquisition. Modes at high frequencies provided a consistent damping factor of PS and PMMA whereas modes below 800 kHz were affected by depth-related artifacts or were coupled lateral and horizontal modes. Overall, FSFV provides a comprehensive set of data that enables the decoupling of IR and mechanical information.

B. PS-LDPE

Now we turn to a more mechanically heterogeneous sample. We acquired maps of the same region of a PS-LDPE sample, at 1468 cm^{-1} using the RE, REFV, and FSFV modes. RE maps were not conclusive as lateral forces applied by the tip led to significant damage to the sample (Fig. 12 in Appendix C). Topography and IR maps are displayed in Fig. 6 for REFV and FSFV, at different repetition rates. Contrasts on IR maps at 1468 cm^{-1} are low due to the overlap of absorption features of LDPE at 1466 cm^{-1} and PS at 1453 cm^{-1} (Figs. 13 and 14 in Appendix D). Therefore, the discussion on this sample will focus on the sensitivity of FSFV and REFV to mechanical heterogeneities and not on IR contrasts. A discussion on IR contrasts is given in Appendix D.

Figure 6 shows the frequency map along a line profile on the sample. The one order of magnitude stiffness difference between

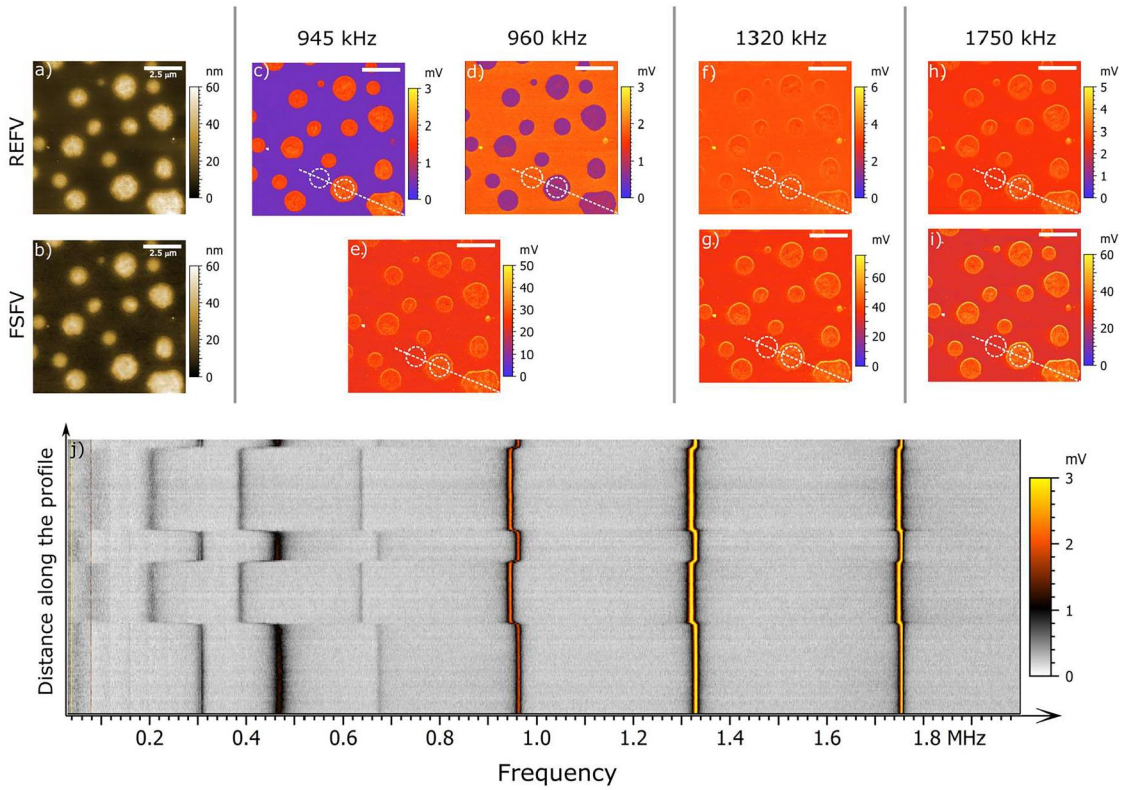

FIG. 6. Maps at 1468 cm^{-1} derived from REFV and FSFV on the PS-LDPE sample for the same sample area. (a) and (b) Topographic images. (c) and (d) REFV amplitude maps from two different REFV measurements with the PLL locked at 945 and 960 kHz, the contact resonances on LDPE and PS, respectively. In the two cases, the PLL failed to follow the frequency shifts when transitioning from LDPE to PS. (e) FSFV amplitude map around 960 kHz. (f)–(i) REFV and FSFV amplitude maps at about 1320 and 1750 kHz. (j) Frequency slice along a line profile over the LDPE matrix and two PS beads. Significant frequency shifts are caused by the difference in stiffness of PS and LDPE. Frequency shifts are more pronounced at lower frequencies.

PS and LDPE results in significant shifts of the resonant frequencies when transitioning from the PS matrix to the LDPE droplets, especially at lower frequencies (e.g., $\Delta f \approx 100$ kHz at the 300 kHz resonance and $\Delta f \approx 80$ kHz at the 480 kHz resonance). This prevents accurate phase tracking by the PLL, impeding the acquisition of IR maps in REFV for frequencies below 1000 kHz. As an illustration of this limitation, we performed two REFV measurements with the PLL (and laser excitation) centered at 945 kHz, the contact resonance of the LDPE droplets, and 960 kHz, the contact resonance for the PS matrix. The hold time was set to 5 ms, and the frequency shifts were bounded to −30 and +20 kHz around the resonance frequency. Despite the relatively low frequency shift of 15 kHz between the two materials, the PLL did not accurately track the phase change and the two REFV acquisitions provided IR maps with inverted contrasts [Fig. 6(c) and 6(d)]. In detail, the IR signal on LDPE is ∼2 mV when the PLL is set up at the LDPE contact resonance at 945 kHz [Fig. 6(c)]. A similar signal strength is observed for PS with the PLL now initialized at the 960 kHz PS contact resonance [Fig. 6(d)]. However, neither individual image (c) nor (d) shows comparable IR absorption between PS and LDPE, but reveals a large and inverted contrast, hence the PLL failed. Above 1000 kHz, the frequency shifts are less pronounced and the signal-to-noise ratio improves, allowing effective phase tracking. Since FSFV does not rely on PLL-based frequency tracking, in general cases, FSFV is the better suited mode for IR mapping of samples with highly heterogeneous stiffnesses and/or low signal-to-noise ratio. Nevertheless, REFV remains suitable for such samples at high resonant frequencies, where frequency shifts are reduced.

AFM-IR measurements on the PS-LDPE sample highlight the importance of suppressing shear forces when analyzing fragile samples. While RE can significantly damage such samples and cannot appropriately provide IR maps, REFV and FSFV are able to operate without apparent damage. The RE acquisition was performed with a scan rate of 0.3 Hz, corresponding to a tip velocity of 3 μm/s. Lowering the scan rate could have improved the sample preservation although it would have significantly increased the acquisition duration. Furthermore, the difference in stiffness of PS and LDPE causes important shifts of the resonance frequencies of the cantilever that are not corrected by the PLL in REFV below 1000 kHz. In such cases, FSFV is the only AFM-IR mode that provides an accurate set of data to derive IR mapping of the PS-LDPE sample, decoupled from its mechanical response.

The current study on PS-PMMA and PS-LDPE explored IR imaging capabilities rather than spectroscopy. FSFV spectroscopy currently mimics RE spectroscopy, i.e., spectra are acquired in a RE-like fashion with the probe resting on the surface in feedback for a longer hold time while the wavelength is tuned. We expect a frequency sweep implementation for spectroscopy to have no effect on a single point spectrum since the same material is probed so that damping does not vary (unless softening/melting is affecting the material, which is in general not desired for all AFM-IR modes). Offset correction can be achieved here by baseline correction of the entire spectrum in post-processing. When comparing point spectra between different materials, we expect the results obtained in our current study for IR images at a fixed wavelength to be representative for a spectrum covering multiple wavelengths.

IV. SUMMARY

Analyses of the two test samples evidenced the interest in force volume acquisition modes. The suppression of shear forces caused by the lateral scanning of the tip on the sample favors both the preservation of the sample and simplifies the nature of the contact interaction in REFV and FSFV compared to RE. In addition, FSFV provides, for the first time, a complete description of the IR-induced thermo-mechanical signal through the frequency sweeping, given a set of contact conditions. Notably, this signal is likely sensitive to variations of the indentation setpoint although we worked at a fixed 32 nm indentation setpoint and did not explore the impact of this parameter on IR mapping. By integrating the frequency spectrum in the vicinity of a resonance mode, we obtain the true IR signal, corrected for damping effects arising from the local sample properties and for amplitude offsets caused by the instrument's electronic noise. As a result, FSFV data can offer enhanced IR contrast compared to RE and REFV, as demonstrated in the PS-PMMA sample.

Since FSFV does not rely on a PLL to track the frequency variations caused by the changing nature of the contact interaction, it can operate in low signal-to-noise ratio conditions. Resonance frequencies of the cantilever are identified at the data-treatment stage prior to the production of IR maps. Frequency sweeps in FSFV can also cover multiple resonant modes allowing multifrequency analyses and AFM-IR-based tomographic reconstruction (Dazzi *et al.*, 2024). Therefore, FSFV is an alternative operating mode not only to resonance-enhanced contact techniques but also to heterodyne detection techniques such as tapping AFM-IR as they rely on frequency tracking mechanisms and they do not provide damping correction (see Table I for a comparison of the investigated AFM-IR techniques and tapping AFM-IR). Still, FSFV scans take significantly longer than classical RE or REFV scans. Given our set of parameters listed in Sec. II B, RE, REFV, and FSFV acquisitions lasted 14, 27, and 240 min, respectively. Those durations notably depend on the scan rate in RE and on the ramp rate and hold time in REFV and FSFV. The relationship between the hold time, the number of sampling points, and the frequency sweep range determines both the duration of the acquisition and the signal-to-noise ratio (Sec. II B). In the case of a frequency sweep, the minimum integration bandwidth is given by the ratio of the number of sampling points over the hold time and the number of integration at each frequency increment is given by the ratio of the frequency over the bandwidth. Therefore, the signal-to-noise ratio is necessarily lower at low frequency than at high frequency, especially when the sweep range is large. Aiming at a target value for the number of integrations at the lower end of the sweep range can help in determining the appropriate operating parameters and will set the acquisition duration. Sweeping over a reduced frequency range may help in decreasing the hold time. However, as large frequency shifts are expected for mechanically heterogeneous samples, it is crucial to select a sweep range large enough to capture shifts induced by stiffness variations. In REFV, the ramp rate has a stronger impact on the overall duration of an acquisition

TABLE I. Summary table of the operational capabilities of RE, REFV, and FSFV. Tapping AFM-IR is an alternative to work on fragile samples but does not allow damping correction. The duration of an acquisition depends on the set of parameters listed in Sec. II. The duration of the acquisitions performed in this study is indicated in parenthesis.

AFM-IR mode	IR mapping	Free of Lateral forces	Cantilever excitation	Damping correction	Amplitude offset correction	Multi-frequency analyses	Frequency-shift correction capabilities	Duration of an acquisition
RE	Yes	No	Linear	No	No	No	PLL	Standard (*14 min*)
REFV	Yes	Yes	Linear	No	No	No	PLL	Slower (*27 min*)
FSFV	Yes	Yes	Linear	Yes	Yes	Yes	Post-processing	Slowest (*240 min*)
Tapping	Yes	Yes	Non-linear	No	No	No	PLL	Standard

given the short hold time compared to FSFV. Modifying the ramp rate will increase or decrease the approach and retract speed. Finally, in RE, the scan rate can be lowered to limit the intensity of shear forces on the samples (e.g., Phan *et al.*, 2024), increasing the IR mapping duration. As an example, RE acquisitions performed with a 0.1 Hz scan rate last about 43 min. Therefore, it is important to assess the nature of a sample and the scientific needs prior to data collection to select the most suited AFM-IR operating mode.

Given its characteristics, the use of FSFV will be crucial in the analysis of fragile, chemically heterogeneous samples, mixing organic and mineral compounds at the nanoscale, such as extraterrestrial grains delivered by asteroid sample return missions (Mathurin *et al.*, 202 4; Phan *et al.*, 2024; and Yabuta *et al.*, 2023), terrestrial coal bearing samples (Phan *et al* ., 2023), model and ancient paint of art pieces (Georgiou *et al.*, 2025; Ma *et al.*, 2022; and Morsch *et al.*, 2017), and preserved archeological textiles (Reynaud *et al.*, 2020). Further technique refinement will focus on the development of standard samples with known mechanical and IR properties that will be used to interpret FSFV measurements on complex samples. Such approach will provide a dataset to eventually reach an enhanced deconvolution of IR and mechanical responses.

AFM-IR is sensitive to both the mechanical and vibrational properties of solids. Infrared nano-spectroscopy, thus, requires the deconvolution of the IR response of the sample and the mechanical coupling between the AFM cantilever and the sample surface. By suppressing shear forces in the tip–sample interaction, force volume modes (REFV and FSFV) allow both to simplify the mechanical interaction and to reduce damage to the sample caused by lateral scanning. Furthermore, by giving access to the full frequency spectrum of the AFM cantilever, FSFV provides a comprehensive set of data to deconvolute the mechanical and IR signals with the aim of improving the accuracy of the IR contrast of the samples. Such advances will enable to address the chemical signatures of samples with increasing chemical and mechanical complexity.

ACKNOWLEDGMENTS

This work was supported by the Paris Ile de-France Region-DIM "Matériaux anciens et patrimoniaux." The research at UMONS is supported by F.R.S.-FNRS F.R.S. Grands Equipments [No. (40007941)-2022] and Projet de Recherche [No. (PDR)-2022 (40007942)].

AUTHOR DECLARATIONS

Conflict of Interest

The authors declare the following competing financial interest(s): P.D.W. and M.W. are employed by Bruker Nano Surfaces Division, a manufacturer of instrumentation and probes for AFM-IR spectroscopy. A.D. is a coinventor of AFM-IR patents licensed to Bruker Nano Surfaces Division.

Author Contributions

J. Rojas: Data curation (equal); Methodology (equal); Writing – original draft (equal). **C. Collange:** Data curation (equal); Methodology (equal); Software (equal). **V. Phan:** Writing – original draft (equal). **P. Nickmilder:** Resources (equal). **Ph. Leclère:** Resources (equal). **P. De Wolf:** Conceptualization (equal); Resources (equal); Writing – original draft (equal). **M. Wagner:** Conceptualization (equal); Resources (equal); Writing – original draft (equal). **A. Deniset-Besseau:** Data curation (equal); Methodology (equal); Writing – original draft (equal). **J. Mathurin:** Data curation (equal); Methodology (equal); Writing – original draft (equal). **A. Dazzi:** Conceptualization (equal); Data curation (equal); Methodology (equal); Supervision (equal); Writing – original draft (equal).

DATA AVAILABILITY

The data that support the findings of this study are available from the corresponding authors upon reasonable request. The processing software for frequency-sweep force volume data developed for this study can be found in Zenodo at https://doi.org/10.5281/zenodo.17936883, Ref. Collange *et al.*, 2025.

APPENDIX A: RESONANCE MODES OF THE CANTILEVER

Frequency-sweep force volume AFM-IR records frequency spectra of the tip–sample interaction at every pixel of an analyzed area. Advanced data processing on the frequency spectra allows

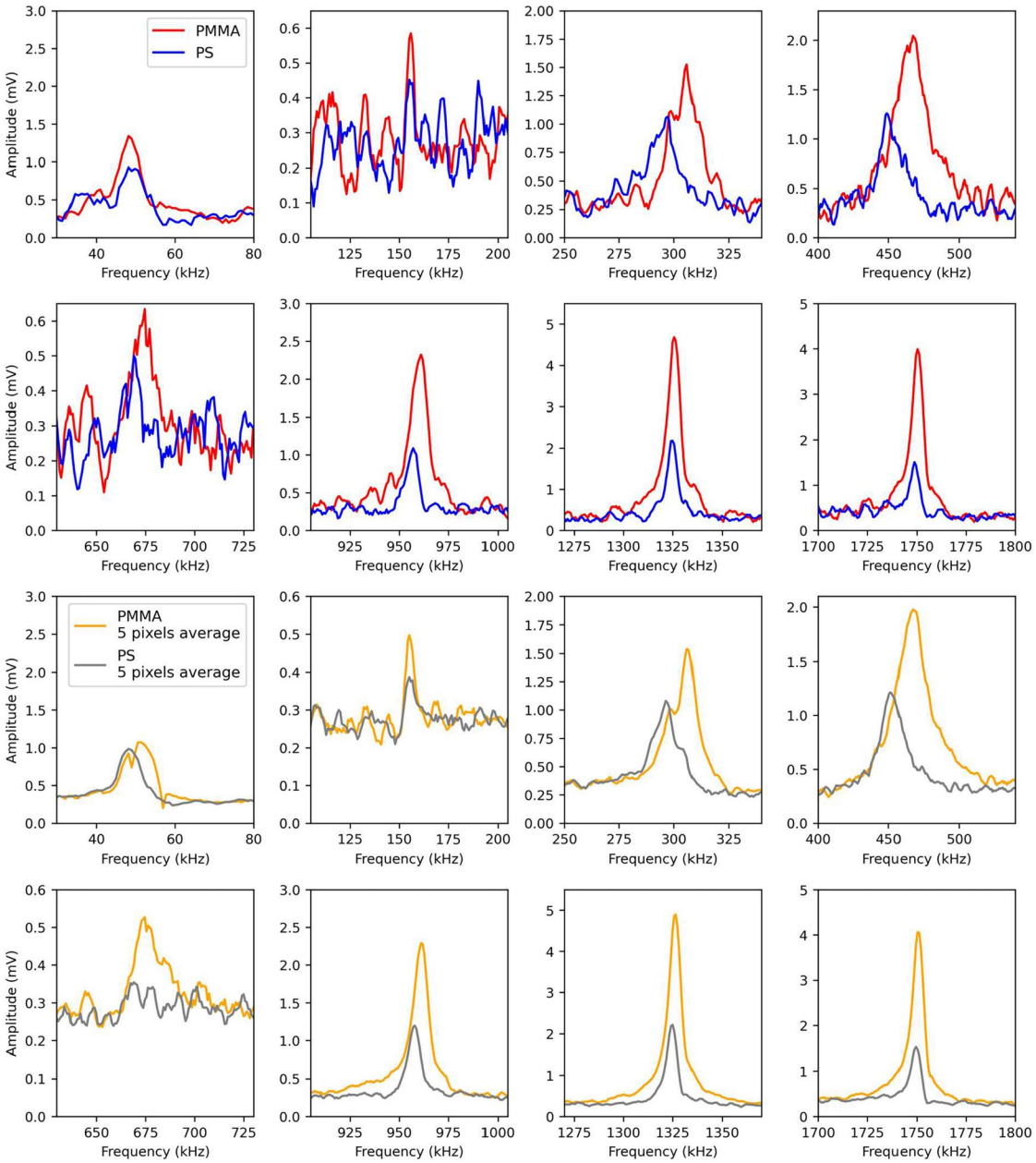

FIG. 7. Frequency spectra around the resonant modes of the tip–sample interaction. First two rows: frequency spectra of a single pixel from the PMMA matrix (red) and a PS bead (blue). Last two rows: frequency spectra averaged on five pixels from the PMMA matrix (orange) and a PS bead (gray). All the spectra were smoothed with a Savitzky–Golay filter of window length 11 and a polynomial order of 3.

one to extract physical parameters, such as the damping coefficient and the integrated amplitude of the signal. Typical frequency spectra around the resonance frequency are displayed in Fig. 7. Frequency sweeps were performed during a 200 ms long hold time. Signal-to-noise ratio of the frequency spectra could be improved by a longer hold time.

APPENDIX B: AFM-IR MAPS OF PS-PMMA AT DIFFERENT RESONANCE FREQUENCIES

Figures 8–11 show AFM-IR maps of the PS-PMMA sample at a wavenumber of 1730 cm^{-1} and resonance frequencies of 310, 490, 960, and 1750 kHz. Maps derived from RE, REFV, and FSFV acquisitions are displayed for each resonance frequency.

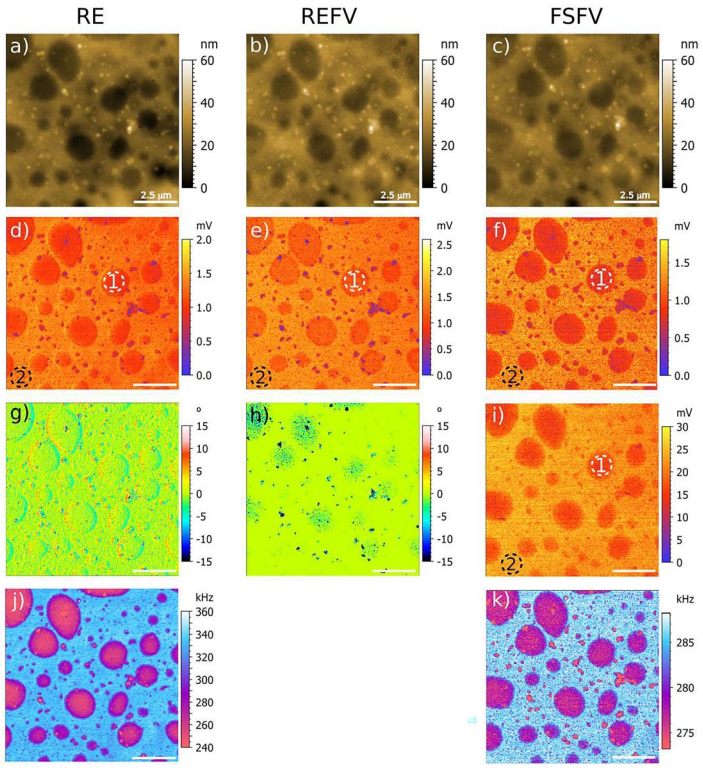

FIG. 8. Maps of the same area derived from RE, REFV, and FSFV modes on the PS-PMMA sample at 310 kHz. First column (RE): (a) topography, (d) maximum IR amplitude at 1730 cm^{-1}, (g) phase, and (j) frequency for RE-contact. Second column (REFV): (b) topography, (e) maximum IR amplitude at 1730 cm^{-1} and (h) phase for REFV. Third column (FSFV): (c) topography, (f) maximum IR amplitude, (i) integrated IR amplitude at 1730 cm^{-1}, and (k) frequency for FSFV. Dotted circles indicate the two regions of interest, which were used to compute the chemical contrasts.

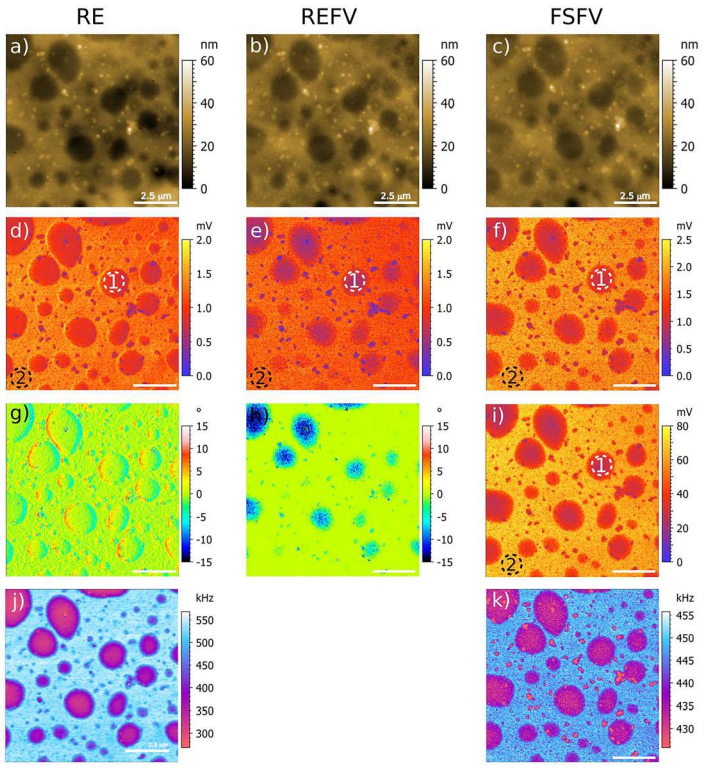

FIG. 9. Maps of the same area derived from RE, REFV, and FSFV modes on the PS-PMMA sample at 490 kHz. First column (RE): (a) topography, (d) maximum IR amplitude at 1730 cm^{-1}, (g) phase and (j) frequency for RE-contact. Second column (REFV): (b) topography, (e) maximum IR amplitude at 1730 cm^{-1} and (h) phase for REFV. Third column (FSFV): (c) topography, (f) maximum IR amplitude, (i) integrated IR amplitude at 1730 cm^{-1} and (k) frequency for FSFV. Dotted circles indicate the two regions of interest, which were used to compute the chemical contrasts.

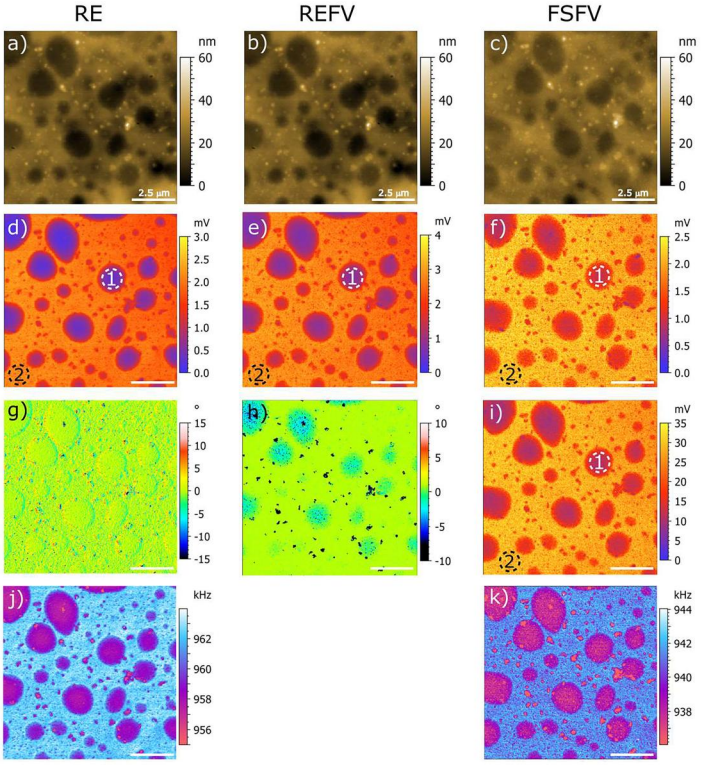

FIG. 10. Maps of the same area derived from RE, REFV, and FSFV modes on the PS-PMMA sample at 960 kHz. First column (RE): (a) topography, (d) maximum IR amplitude at 1730 cm^{-1}, (g) phase and (j) frequency for RE-contact. Second column (REFV): (b) topography, (e) maximum IR amplitude at 1730 cm^{-1} and (h) phase for REFV. Third column (FSFV): (c) topography, (f) maximum IR amplitude, (i) integrated IR amplitude at 1730 cm^{-1}, and (k) frequency for FSFV. Dotted circles indicate the two regions of interest, which were used to compute the chemical contrasts.

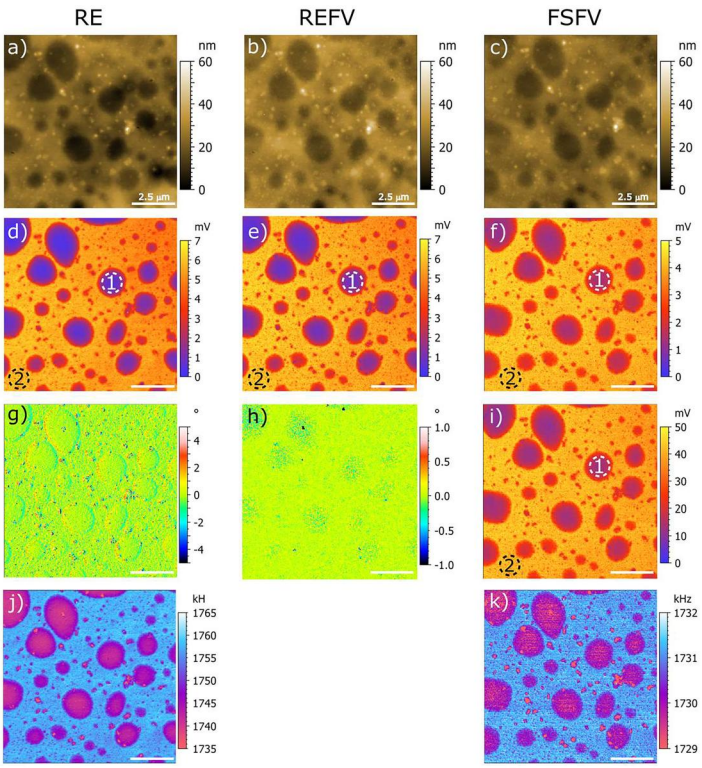

FIG. 11. Maps of the same area derived from RE, REFV, and FSFV modes on the PS-PMMA sample at 1750 kHz. First column (RE): (a) topography, (d) maximum IR amplitude at 1730 cm^{-1}, (g) phase and (j) frequency for RE-contact. Second column (REFV): (b) topography, (e) maximum IR amplitude at 1730 cm^{-1}, and (h) phase for REFV. Third column (FSFV): (c) topography, (f) maximum IR amplitude, (i) integrated IR amplitude at 1730 cm^{-1}, and (k) frequency for FSFV. Dotted circles indicate the two regions of interest, which were used to compute the chemical contrasts.

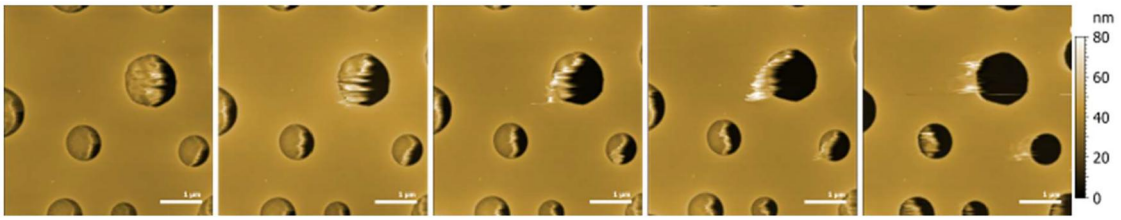

FIG. 12. Succession of topographic images of the PS-LDPE sample acquired in RE AFM-IR mode. LDPE droplets are being scratched by the scanning tip, preventing the RE analysis.

APPENDIX C: RESONANCE-ENHANCED AFM-IR ON PS-LDPE

Successive RE measurements on the PS-LDPE sample, with a force of 3 nN, are displayed in Fig. 12. The shear forces inherent to RE caused the progressive destruction of the soft LDPE droplets. Therefore, no meaningful AFM-IR data can be extracted from those RE measurements.

APPENDIX D: IR CONTRAST ON PS-LDPE

Infrared contrasts at 1468 cm^{-1} for the PS-LDPE sample are defined similarly to the contrast at 1730 cm^{-1} for the PS-PMMA (Sec. III A). Amplitude contrasts in the 1468 cm^{-1} FSFV and REFV maps are noted C_{FSFV} and C_{REFV}, respectively, in this section. The integrated amplitude contrast derived from FSFV is noted $\tilde{C}_{FSFV}$.

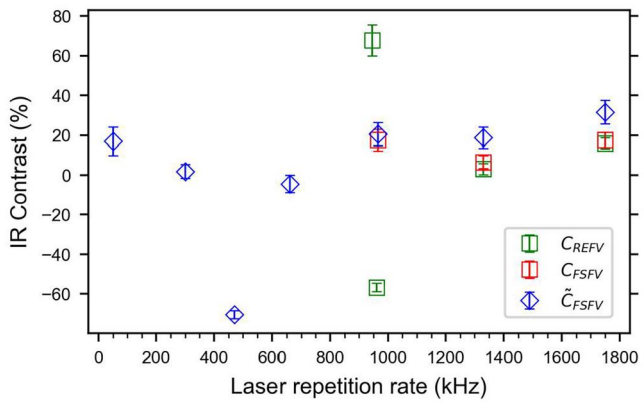

FIG. 13. PS-LDPE contrast at 1468 cm^{-1} measured for different laser repetition rates. Green squares and red squares are derived from the maximum amplitude maps of REFV and FSFV. Blue diamonds are derived from the integrated amplitude maps of FSFV.

Regions of interest used to compute the infrared contrasts are represented in Fig. 6 by white dotted circles. All the contrasts measured at different repetition rates are displayed in Fig. 13. For resonant frequencies below 1000 kHz (at 50, 300, 470, 670, and 950 kHz), the PLL in REFV fails to accurately track the frequency shifts [Fig. 6(j)]. Although, at 950 kHz, the frequency shift between LDPE and PS is only about 15 kHz, the PLL does not manage to track the resonance. We intended to initialize the PLL on the frequencies of both LDPE (945 kHz) and PS (960 kHz) without any positive impacts on the accuracy of the tracking. Modifying the starting frequency (945 or 960 kHz) results in two IR amplitude maps with inverted contrast of 70% and −60% [Figs. 6(c), 6(d), and 13]. Above 1000 kHz, the lower frequency shift allows an accurate tracking by the PLL. For those frequencies (1320 and 1750 kHz), the integrated FSFV contrast is higher than the maximum amplitude contrast from FSFV and REFV. As expected, the baseline subtraction and the integration of the resonance width led to an enhancement of the contrast. However, integrated FSFV contrasts measured on the PS-LDPE sample are lower than contrasts measured on the PS-PMMA sample with values ranging from about 0 to 40% and of −70% at 470 kHz. Such low contrast may be impacted by the proximity of the LDPE and PS IR bands at 1468 and 1450 cm^{-1}. The overlap of the LDPE and PS IR bands (Fig. 14) induces a non-zero signal over the PS matrix in the 1468 cm^{-1} IR map that lowers the LDPE-PS contrast. In parallel, the limited thickness possibly impacts the intensity of the IR signal and the associated contrast. As shown in the topographic map of the PS-LDPE sample (Fig. 12), the PS matrix is about 35 nm thick, and the LDPE droplets are about 70 nm thick. Both LDPE droplets and PS matrix are deposited on a Si substrate. This thickness limits the intensity of the AFM-IR signal. Additionally, the presence of the Si substrate leads to the reflection of the IR light and/or to the attenuation of the IR-induced mechanical signal. The combination of those effects limits the accuracy of the IR contrast at a low repetition rate on the PS-LDPE sample.

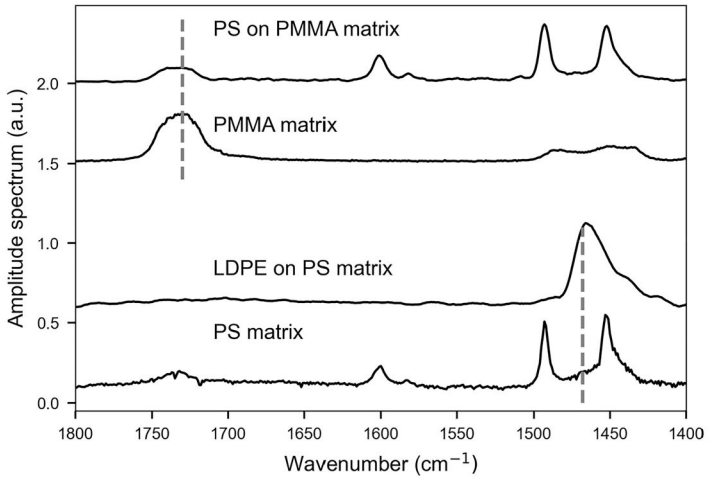

FIG. 14. IR spectra of the two test samples acquired during REFV acquisitions, vertically shifted for clarity. Top two spectra: AFM-IR spectra of PS islands embedded into the PMMA matrix and of the PMMA matrix. The absorption at 1730 cm^{-1} is due to the PMMA matrix and is still probed while measuring on a PS bead. Bottom two spectra: AFM-IR spectra of the LDPE droplets within the PS matrix and of the PS matrix. The absorption at 1468 cm^{-1} is attributed to LDPE and overlaps with the 1450 cm^{-1} absorption of PS.

APPENDIX E: FSFV DATA TREATMENT APPLICATION

In the following, we describe the FSFV data processing using our in-house developed python-based application (Collange *et al.*, 2025). The data obtained in FSFV are data cubes, i.e., for a given wavenumber, every pixel contains a frequency spectrum of the tip-sample interaction. Data cubes are indexed by the triplet (m, n, f), i.e., their coordinates along the x and y positions and the frequency value f.

The data processing follows three steps: (i) smoothing the data and subtracting the (electronic) offset, (ii) identifying the resonance frequencies, and (iii) extracting the parameters associated with the resonances.

A. Smoothing and offset subtraction

First, the user can apply a Savitzky–Golay filter to smooth the data with the desired parameters (default parameters are a 11 units-wide window and a polynomial order of 3). Default parameters should be adjusted to the frequency resolution of the data in order to preserve the data integrity. An example of the smoothing operation is shown in Fig. 15, with the raw and smoothed frequency spectrum in blue and red, respectively. Those data are derived from the data cube at 1730 cm^{-1} on the PS-PMMA sample, at the (m = 0, n = 0) position (first entry of the first column). Once validated by the user, the smoothing is performed on all frequency spectra of the dataset.

An electronic offset can affect the data and cause a non-zero signal where no signal is expected. The users can define a custom frequency range, far from the resonance modes, where the offset will be evaluated for each frequency spectrum (i.e., for each pixel) by averaging the signal over the frequency range. Subsequently, the users can choose between subtracting this offset or subtracting a constant user-defined offset.

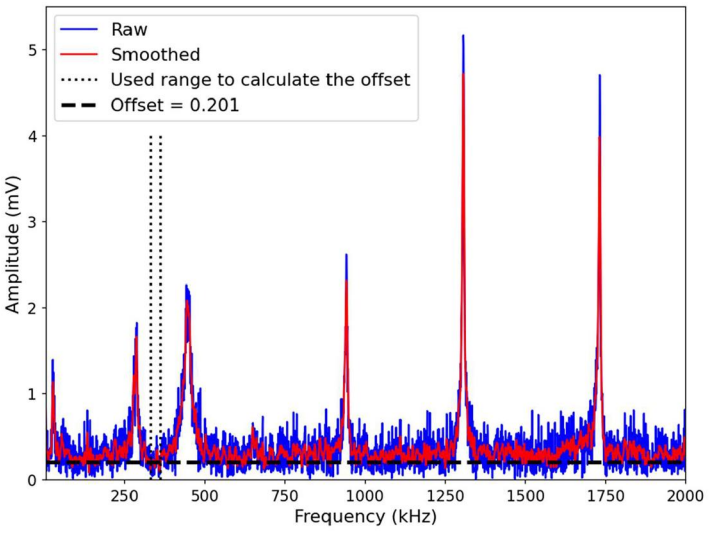

FIG. 15. Raw (in blue) vs. smoothed (in red) frequency spectrum at the (0, 0) position of the data cube at 1730 cm^{-1} on the PS-PMMA sample.

After the offset subtraction, the application returns a 2D map of the offset value at each pixel and a 2D map of the integrated spectra over the whole frequency range.

B. Identifying the resonance frequencies

Once the data have been smoothed and offset-corrected, the application offers to visualize the data through an interactive interface in order to identify the resonance modes. Figure 16 shows a typical visualization of the dataset with the topography map (a), here processed with the MountainsLab software, a slice of the data cube along the y axis at the position m = 128 (b), a slice of the data cube along the x axis at the position n = 128 (c), and a zoomed-in map of a user-defined frequency range (d). Users can visualize different cube slices by clicking on different positions in the topography map, where dashed lines indicate the location of the cross sections. In the slices presented in Figs. 16(b) and 16(c), seven resonant frequencies are visible around 136, 286, 450, 655, 943, 1310, and 1730 kHz, for the PS-PMMA sample at 1730 cm^{-1}. Based on this visualization, users can evaluate the magnitude of the frequency shifts over the sample for each mode.

C. Extraction of the resonance modes parameter

Once all the resonance modes are identified, the user can opt to either directly measure the parameters of the modes (resonance frequency, maximum amplitude, full width at half maximum, integral) on the smoothed data or to perform a DSHO fit to the smoothed data and to extract the parameters from the fit.

In both cases, the user has to define a set of input values for each resonance mode n to process (Table II):

- Central frequency f_c (kHz) of the nth mode: used to label the resulting files.
- Minimal frequency f_{min} (kHz) and maximal frequency f_{max} (kHz): frequency range over which the maximum value of the spectra will be searched. For the DSHO fitting procedure, the central frequency is used as the initial parameter of the fit.

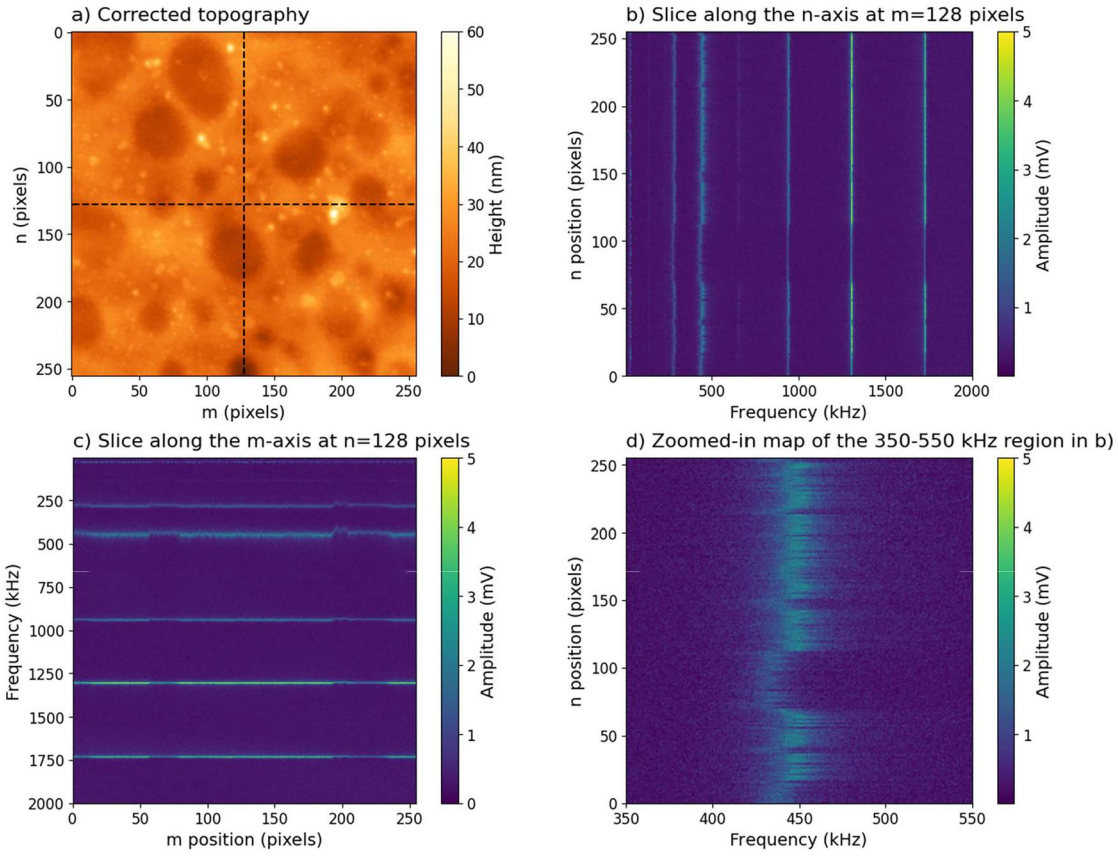

FIG. 16. (a) Corrected topography (processed with MountainsLab) with the cross section at position m = 128 (vertical dashed line) and n = 128 pixels (horizontal dashed line). Slices along the (b) n- and (c) m-axis of the data cube at 1730 cm^{-1} on the PS-PMMA sample, corresponding to the cross section represented in panel (a). (d) Zoomed-in region of the frequency range from 350 to 550 kHz of panel (b).

TABLE II. Parameters for each resonance in the data cube at 1730 cm^{-1} on the PS-PMMA sample. The mode no. specifies modes that the user wants to fit and does not reflect the numbering of the eigen modes.

Mode no.	1	2	3	4	5	6	7
Central frequency (kHz)	136	286	450	655	943	1310	1730
Minimal frequency (kHz)	120	260	410	600	920	1290	1720
Maximal frequency (kHz)	150	300	480	685	970	1330	1750
Amplitude threshold (mV)	0	0	0	0	0	0	0
Accepted shift of the central frequency (kHz)	5	10	10	5	5	5	5
Fitting range (kHz)	100	100	150	50	100	150	150
Multiple N of the largest FWHM	2	2	2	2	2	2	2
Maximum FWHM threshold (kHz)	30	30	30	30	30	30	30

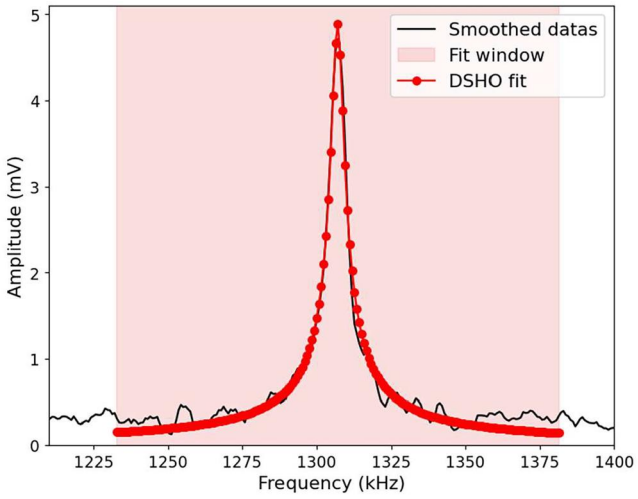

FIG. 17. Results of the DSHO fit on the smoothed data (black line), performed over the fit window (light red area) are shown with the red dots and line.

- Amplitude threshold d_{noise} (mV): threshold below which the maximum value of the signal at a position (n, m) is considered noise. No further evaluation is performed if the maximum value of the signal is below the threshold and output parameters are NaN values.
- Accepted shift of the central frequency δf (kHz) (only for the DSHO fit): maximum frequency shift below which the resonant frequency will be searched for. The DSHO fit will look for a resonance value in the interval $(f_c - \delta f; f_c + \delta f)$. This restricts the calculated central frequency resonance around the initial central frequency.
- Fitting range Δf (kHz) (only for the DSHO fit): frequency range centered around the resonance frequency f_n, used to perform the fit. To accurately fit the data, users should make sure that neighboring resonance modes n − 1 and n + 1 are not included in the fitting range. The damping coefficient for the DSHO fit is initialized based on the measured FWHM: $\Gamma_{init} = 2\pi\sigma_{init}/\sqrt{3}$.

Additional inputs are then asked in order to compute the integral of the signal around a resonance mode, for each pixel (m, n). The procedure relies on integrating all the frequency spectra over the same frequency range $[f_n - \Delta f/2; f_n + \Delta f/2]$ centered around the resonance frequency f_n of the nth mode, determined directly from the data or by the fitting procedure. Noticeably, as f_n can differ from one pixel to another, the integration range is not fixed but its length is constant, equal to Δf.

- **Multiple N of the largest FWHM used to define the integration interval:** in this option, the fitting range Δf is automatically determined. The routine will find the widest resonance peak within the data cube (i.e., the resonance with the largest FWHM) and measure its FWHM σ_{max}. The range of integration around the central value f_n is then defined as N times this FWHM, such as $\Delta f = N{\cdot}\sigma_{max}$ and $[f_n - N{\cdot}\sigma_{max}/2; f_n + N{\cdot}\sigma_{max}/2]$.
- **Maximum FWHM threshold (kHz)**: threshold of the maximum FWHM measured in the dataset. As the width of the integration window depends on the largest FWHM value found among the damping result ($\Delta f = N{\cdot}\sigma_{max}$), if the largest FWHM is too wide, then the integral of the resonance mode can include neighboring resonance modes. The maximum FWHM threshold allows to restrict the search for the maximum FWHM to values below the threshold.

The results obtained after the fitting with the parameters of the 6th mode for the data cube at 1730 cm^{-1} on the PS-PMMA sample, at the n = 0 and m = 0 pixel are shown in Fig. 17. The DSHO fit [Eq. (1)] give a maximal amplitude of 4.89 mV, a damping of 4.44 kHz, a central frequency of 1306.96 kHz, and a score fit of $R^2 = 0.978$.

The application returns the following 2D maps, for each resonance mode, derived from direct measurements on the frequency spectra:

- 2D map of the resonance frequency f_n
- 2D map of the FWHM σ_n
- 2D map of the maximum amplitude corrected from the offset $A_{max,corr}$
- 2D map of the integrated signal $\tilde{A}$

The DSHO fitting procedure returns the following 2D maps:

- 2D map of the resonance frequency f_n
- 2D map of the damping coefficient Γ
- 2D map of the maximum amplitude corrected for the offset $A_{max,DSHO}$
- 2D map of the integrated DSHO fit $\tilde{A}_{DSHO}$
- 2D map of the R^2

- Notably, if the condition $\frac{\omega_n}{\Gamma} \gg 1$ is met, the 2D map of the damping coefficient and the 2D map of the FWHM multiplied by $2\pi/\sqrt{3}$ should be equal.

APPENDIX F: ELEMENTS OF THE ANALYTIC AND NUMERIC ANALYSIS OF THE DAMPED SIMPLE HARMONIC OSCILLATOR MODEL

The amplitude of single resonance modes of the tip–sample interaction can be modeled with the characteristic function of the damped simple harmonic oscillator (DSHO),

$$A(\omega) = \frac{B_n(v)}{\sqrt{\left(\omega_n^2 - \omega^2\right)^2 + (\Gamma\omega)^2}}. \tag{F1}$$

By computing the first derivative of the DHSO function, one gets the maximum amplitude $A_{\max}$,

$$A_{\max} = A(\omega_{\max}) = \frac{B_n(v)}{\sqrt{\omega_n^2\Gamma^2 - \frac{\Gamma^4}{4}}} \quad \text{with } \omega_{\max} = \omega_n\sqrt{1 - \frac{\Gamma^2}{2\omega_n^2}}.$$

Then, the expression of the full width at half maximum (FWHM) is derived by solving the equation

$$A(\omega) = \frac{A_{\max}}{2}, \tag{F2}$$

which can be written as

$$\omega^4 + \omega^2\left(\Gamma^2 - 2\omega_n^2\right) + \omega_n^4 - 4\Gamma^2\omega_n^2 + \Gamma^4 = 0\ . \tag{F3}$$

By introducing the variable $X = \omega^2$, one arrives at the two real roots ω_+ and ω_- of this equation

$$\omega_+ = \sqrt{\frac{2\omega_n^2 - \Gamma^2 + \sqrt{12\Gamma^2\omega_n^2 - 3\Gamma^4}}{2}}, \tag{F4}$$

$$\omega_- = \sqrt{\frac{2\omega_n^2 - \Gamma^2 - \sqrt{12\Gamma^2\omega_n^2 - 3\Gamma^4}}{2}}. \tag{F5}$$

Thus, the FWHM σ_ω can be expressed as

$$\sigma_\omega^2 = (\omega_+ - \omega_-)^2\ , \tag{F6}$$

which gives

$$\sigma_\omega = \omega_n\sqrt{2\left(1 - \frac{\Gamma^2}{2\omega_n^2} - \sqrt{1 - 4\frac{\Gamma^2}{\omega_n^2} + \frac{\Gamma^4}{\omega_n^4}}\right)}. \tag{F7}$$

The value of the FWHM depends on the ratio of the damping factor Γ and the eigenfrequency ω_n. In the condition $\frac{\Gamma}{\omega_n} \ll 1$, i.e., the damping factor is very small compared to the eigenfrequency, the equation is simplified to

$$\sigma_\omega \approx \sqrt{3}\Gamma\ , \tag{F8}$$

$$\sigma_f \approx \frac{\sqrt{3}\Gamma}{2\pi}. \tag{F9}$$

Hence, if the resonant mode of the tip–sample interaction can be fitted to a DSHO profile, and in the limit of $\frac{\Gamma}{\omega_n} \ll 1$, the FWHM of the resonant mode is proportional to the damping factor Γ.

Contrarily to Lorentzian profiles, DSHO profiles do not have a finite integral over the real axis. Moreover, the DHSO integral over a bounded interval $[f_n - \Delta f/2\ ;\ f_n + \Delta f/2]$ has a complex analytical expression. Therefore, we performed a numerical simulation to derive a simplified expression of the DSHO integral $\tilde{A}$ for varying Γ, a fixed resonance mode ω_n, in the limit $\frac{\Gamma}{\omega_n} \ll 1$.

In those conditions, one finds

$$\tilde{A} = \int_{f_n - \frac{\Delta f}{2}}^{f_n + \frac{\Delta f}{2}} A(f,\ \omega_n, \Gamma)df = A_{\max}(\Gamma)\cdot\Gamma\cdot\alpha\left(\frac{\Delta f}{\Gamma}\right), \tag{F10}$$

where $\alpha(\Delta f/\Gamma)$ is an increasing function of $\Delta f/\Gamma$. The function α only depends on the $\Delta f/\Gamma$ ratio. We analyzed its behavior by computing the integrals of a set of synthetic DHSO profiles with varying damping Γ and integration range Δf (Fig. 18).

For two materials of respective damping Γ_1 and Γ_2, and for a fixed integration range Δf large enough ($\Delta f \geq \sigma_{f1}$ and $\Delta f \geq \sigma_{f2}$), α verifies

$$\frac{\Gamma_1}{\Gamma_2} \times \frac{\alpha(\Delta f/\Gamma_1)}{\alpha(\Delta f/\Gamma_2)} > 1 \quad \text{if } \frac{\Gamma_1}{\Gamma_2} > 1,$$

$$\frac{\Gamma_1}{\Gamma_2} \times \frac{\alpha(\Delta f/\Gamma_1)}{\alpha(\Delta f/\Gamma_2)} < 1 \quad \text{if } \frac{\Gamma_1}{\Gamma_2} < 1.$$

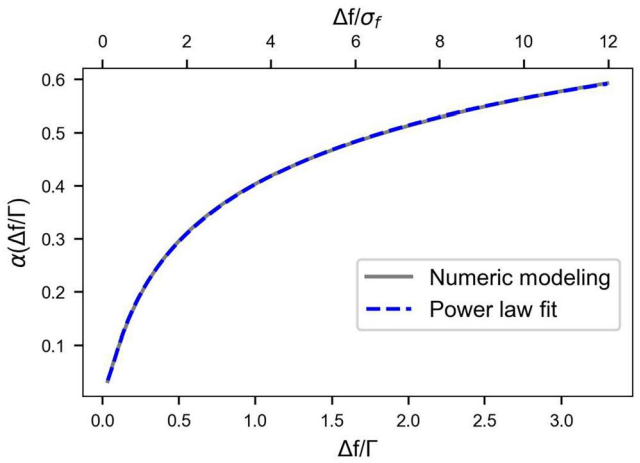

FIG. 18. Evolution of the function $\alpha\left(\frac{\Delta f}{\Gamma}\right)$. The gray curve labeled "numeric modeling" is computed on a set of synthetic DSHO profiles of parameters $\Gamma = 30$, $f_n = 1000$ and Δf ranging from 1 to 100. This function is fitted by a power law (blue dashed curve).

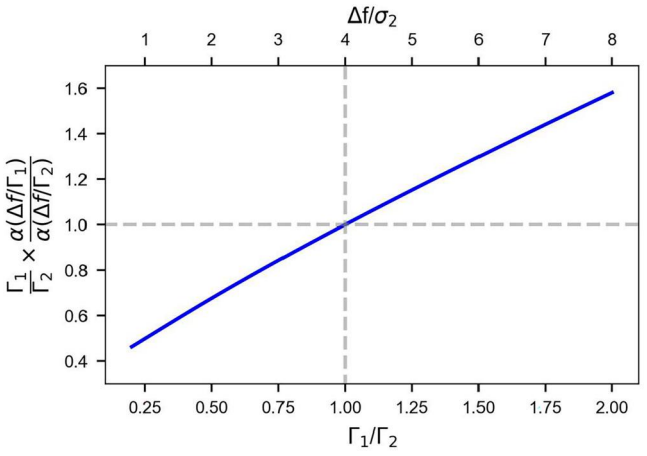

FIG. 19. Evolution of the ratio $\frac{\Gamma_1}{\Gamma_2} \times \frac{\alpha(\Delta f/\Gamma_1)}{\alpha(\Delta f/\Gamma_2)}$ for different values of $\frac{\Gamma_1}{\Gamma_2}$ and for $\Delta f = 4\sigma_1$.

Figure 19 displays the behavior of the $\frac{\Gamma_1}{\Gamma_2} \times \frac{\alpha(\Delta f/\Gamma_1)}{\alpha(\Delta f/\Gamma_2)}$ ratio for varying damping ratios $\frac{\Gamma_1}{\Gamma_2}$ and a fixed integration range $\Delta f = 4\sigma_1$.

Thus, for two materials labeled 1 and 2, if

$$\frac{\widetilde{A_1}}{\widetilde{A_2}} > \frac{A_{\max,1}}{A_{\max,2}} \quad \text{then} \quad \frac{\Gamma_1}{\Gamma_2} > 1.$$

REFERENCES

Collange, C., Dazzi, A., and Mathurin, J., 2025. "Data processing for frequency-sweep force volume AFM-IR," Zenodo. https://doi.org/10.5281/zenodo.17936884

Dartois, E., Engrand, C., Duprat, J., Godard, M., Charon, E., Delauche, L., Sandt, C., and Borondics, F., "Dome C ultracarbonaceous Antarctic micrometeorites: Infrared and Raman fingerprints," A&A **609**, A65 (2018).

Dazzi, A., Glotin, F., and Carminati, R., "Theory of infrared nanospectroscopy by photothermal induced resonance," J. Appl. Phys. **107**, 124519 (2010).

Dazzi, A., Mathurin, J., Leclere, P., Nickmilder, P., De Wolf, P., Wagner, M., Hu, Q., and Deniset-Besseau, A., "Photothermal AFM-IR depth sensitivity: An original pathway to tomographic reconstruction," Anal. Chem. **96**, 17931–17940 (2024).

Dazzi, A., Palmino, F., Deniset-Besseau, A., Mathurin, J., Luzet, V., De Wolf, P., Hu, Q., Li, C., Phillips, C., and Chérioux, F., "Chemical mapping of supramolecular self-assembled monolayers via atomic force microscopy-based infrared with a nanometer-scale lateral resolution," J. Phys. Chem. Lett. **16**, 3433–3437 (2025).

Dazzi, A., Prazeres, R., Glotin, F., and Ortega, J. M., "Local infrared microspectroscopy with subwavelength spatial resolution with an atomic force microscope tip used as a photothermal sensor," Opt. Lett. **30**, 2388–2390 (2005).

Georgiou, R., Dazzi, A., Mathurin, J., Duce, C., Dietemann, P., Thoury, M., and Bonaduce, I., "Nanoscale probing of the organic binder in artists' paint layers: Organic phases and chemical heterogeneity," ACS Appl. Mater. Interfaces **17**, 8464–8473 (2025).

Lu, F., Jin, M., and Belkin, M. A., "Tip-enhanced infrared nanospectroscopy via molecular expansion force detection," Nat. Photonics **8**, 307–312 (2014).

Ma, X., Pavlidis, G., Dillon, E., Beltran, V., Schwartz, J. J., Thoury, M., Borondics, F., Sandt, C., Kjoller, K., Berrie, B. H., and Centrone, A., "Micro to nano: Multiscale IR analyses reveal zinc soap heterogeneity in a 19th-century painting by corot," Anal. Chem. **94**, 3103–3110 (2022).

Mathurin, J., Bejach, L., Dartois, E., Engrand, C., Dazzi, A., Deniset-Besseau, A., Duprat, J., Kebukawa, Y., Yabuta, H., Bonal, L., Quirico, E., Sandt, C., Borondics, F., Barosch, J., Beck, P., Cody, G. D., De Gregorio, B. T., Hashiguchi, M., Kilcoyne, D. A. L., Komatsu, M., Martins, Z., Matsumoto, M., Montagnac, G., Mostefaoui, S., Nittler, L. R., Ohigashi, T., Okumura, T., Phan, V. T. H., Remusat, L., Sandford, S., Shigenaka, M., Stroud, R., Suga, H., Takahashi, Y., Takeichi, Y., Tamenori, Y., Verdier-Paoletti, M., Yamashita, S., Nakamura, T., Morita, T., Kikuiri, M., Amano, K., Kagawa, E., Noguchi, T., Naraoka, H., Okazaki, R., Sakamoto, K., Yurimoto, H., Abe, M., Kamide, K., Miyazaki, A., Nakato, A., Nakazawa, S., Nishimura, M., Okada, T., Saiki, T., Tachibana, S., Tanaka, S., Terui, F., Tsuda, Y., Usui, T., Watanabe, S., Yada, T., Yogata, K., and Yoshikawa, M., "AFM-IR nanospectroscopy of nanoglobule-like particles in Ryugu samples returned by the Hayabusa2 mission," A&A **684**, A198 (2024).

Mathurin, J., Deniset-Besseau, A., Bazin, D., Dartois, E., Wagner, M., and Dazzi, A., "Photothermal AFM-IR spectroscopy and imaging: Status, challenges, and trends," J. Appl. Phys. **131**, 010901 (2022).

Mathurin, J., Pancani, E., Deniset-Besseau, A., Kjoller, K., Prater, C. B., Gref, R., and Dazzi, A., "How to unravel the chemical structure and component localization of individual drug-loaded polymeric nanoparticles by using tapping AFM-IR," Analyst **143**, 5940–5949 (2018).

Morsch, S., van Driel, B. A., van den Berg, K. J., and Dik, J., "Investigating the photocatalytic degradation of oil paint using ATR-IR and AFM-IR," ACS Appl. Mater. Interfaces **9**, 10169–10179 (2017).

Phan, V. T. H., Beck, P., Rebois, R., Quirico, E., Noguchi, T., Matsumoto, T., Miyake, A., Igami, Y., Haruta, M., Saito, H., Hata, S., Seto, Y., Miyahara, M., Tomioka, N., Ishii, H. A., Bradley, J. P., Ohtaki, K. K., Dobrică, E., Leroux, H., Le Guillou, C., Jacob, D., De La Peña, F., Laforet, S., Marinova, M., Langenhorst, F., Harries, D., Abreu, N. M., Gray, J., Zega, T., Zanetta, P., Thompson, M. S., Stroud, R., Mathurin, J., Dazzi, A., Dartois, E., Engrand, C., Burgess, K., Cymes, B. A., Bridges, J. C., Hicks, L., Lee, M. R., Daly, L., Bland, P. A., Zolensky, M. E., Frank, D. R., Martinez, J., Tsuchiyama, A., Yasutake, M., Matsuno, J., Okumura, S., Mitsukawa, I., Uesugi, K., Uesugi, M., Takeuchi, A., Sun, M., Enju, S., Takigawa, A., Michikami, T., Nakamura, T., Matsumoto, M., Nakauchi, Y., Abe, M., Nakazawa, S., Okada, T., Saiki, T., Tanaka, S., Terui, F., Yoshikawa, M., Miyazaki, A., Nakato, A., Nishimura, M., Usui, T., Yada, T., Yurimoto, H., Nagashima, K., Kawasaki, N., Sakamotoa, N., Hoppe, P., Okazaki, R., Yabuta, H., Naraoka, H., Sakamoto, K., Tachibana, S., Watanabe, S., and Tsuda, Y., "*In situ* investigation of an organic micro-globule and its mineralogical context within a Ryugu 'sand' grain," Meteorit. Planet. Sci. **59**, 1983–2001 (2024).

Phan, V. T. H., Rebois, R., Beck, P., Quirico, E., Noguchi, T., and Takase, M., "Chemical functional characterization of immature and mature coals at the nanoscale by atomic force microscopy-based infrared spectroscopy (AFM-IR)," Int. J. Coal Geol. **267**, 104196 (2023).

Rabe, U., "Atomic force acoustic microscopy," in *Applied Scanning Probe Methods II: Scanning Probe Microscopy Techniques*, edited by B. Bhushan and H. Fuchs (Springer, Berlin, 2006), pp. 37–90.

Reynaud, C., Thoury, M., Dazzi, A., Latour, G., Scheel, M., Li, J., Thomas, A., Moulhérat, C., Didier, A., and Bertrand, L., "In-place molecular preservation of cellulose in 5,000-year-old archaeological textiles," Proc. Natl. Acad. Sci. U.S.A. **117**, 19670–19676 (2020).

Tuteja, M., Kang, M., Leal, C., and Centrone, A., "Nanoscale partitioning of paclitaxel in hybrid lipid–polymer membranes," Analyst **143**, 3808–3813 (2018).

Wagner, M., Hu, Q., Hu, S., Phillips, C., Wang, W., Pittenger, B., Fali, A., Li, C., Mathurin, J., Dazzi, A., Su, C., and De Wolf, P., "Force volume atomic force microscopy–infrared for simultaneous nanoscale chemical and mechanical spectromicroscopy," ACS Nano **19**, 18791–18803 (2025).

Wang, L., Wagner, M., Wang, H., Pau-Sanchez, S., Li, J., Edgar, J. H., and Xu, X. G., "Revealing phonon polaritons in hexagonal boron nitride by multi-pulse peak force infrared microscopy," Adv. Opt. Mater. **8**, 1901084 (2020).

Wang, L., Wang, H., and Xu, X. G., "Principle and applications of peak force infrared microscopy," Chem. Soc. Rev. **51**, 5268–5286 (2022).

Yabuta, H., Cody, G.D., Engrand, C., Kebukawa, Y., De Gregorio, B., Bonal, L., Remusat, L., Stroud, R., Quirico, E., Nittler, L., Hashiguchi, M., Komatsu, M., Okumura, T., Mathurin, J., Dartois, E., Duprat, J., Takahashi, Y., Takeichi, Y., Kilcoyne, D., Yamashita, S., Dazzi, A., Deniset-Besseau, A., Sandford, S., Martins, Z., Tamenori, Y., Ohigashi, T., Suga, H., Wakabayashi, D., Verdier-Paoletti, M., Mostefaoui, S., Montagnac, G., Barosch, J., Kamide, K., Shigenaka, M., Bejach, L., Matsumoto, M., Enokido, Y., Noguchi, T., Yurimoto, H., Nakamura, T., Okazaki, R., Naraoka, H., Sakamoto, K., Connolly, H.C., Lauretta, D.S., Abe, M., Okada, T., Yada, T., Nishimura, M., Yogata, K., Nakato, A., Yoshitake, M., Iwamae, A., Furuya, S., Hatakeda, K., Miyazaki, A., Soejima, H., Hitomi, Y., Kumagai, K., Usui, T., Hayashi, T., Yamamoto, D., Fukai, R., Sugita, S., Kitazato, K., Hirata, N., Honda, R., Morota, T., Tatsumi, E., Sakatani, N., Namiki, N., Matsumoto, K., Noguchi, R., Wada, K., Senshu, H., Ogawa, K., Yokota, Y., Ishihara, Y., Shimaki, Y., Yamada, M., Honda, C., Michikami, T., Matsuoka, M., Hirata, Naoyuki, S., Arakawa, M., Okamoto, C., Ishiguro, M., Jaumann, R., Bibring, J.-P., Grott, M., Schröder, S., Otto, K., Pilorget, C., Schmitz, N., Biele, J., Ho, T.-M., Moussi-Soffys, A., Miura, A., Noda, H., Yamada, T., Yoshihara, K., Kawahara, K., Ikeda, H., Yamamoto, Y., Shirai, K., Kikuchi, S., Ogawa, N., Takeuchi, H., Ono, G., Mimasu, Y., Yoshikawa, K., Takei, Y., Fujii, A., Iijima, Y., Nakazawa, S., Hosoda, S., Iwata, T., Hayakawa, M., Sawada, H., Yano, H., Tsukizaki, R., Ozaki, M., Terui, F., Tanaka, S., Fujimoto, M., Yoshikawa, M., Saiki, T., Tachibana, S., Watanabe, S., Tsuda, Y., Macromolecular organic matter in samples of the asteroid (162173) Ryugu. Science **379**, eabn9057 (2023).